DOI: https://10.83080/rejost.vol6no8.329

Researchers Journal of Science and Technology (REJOST)

A Hybrid AHP-Entropy and K-Means DRASTIC Framework for Geoelectrical-Based Groundwater Vulnerability Mapping in Akwa Ibom State, Nigeria

Ettiabasi B. Umoren*, Aniekan M. Ekanem, Nyakno J. George and Jewel E. Thomas

Abstract

The assessment of groundwater vulnerability to anthropogenic contamination is critical for water resource management, yet traditional empirical overlay index models like DRASTIC suffer from rigid subjective weightings and arbitrary hazard classifications that fail to capture spatial heterogeneity. To overcome these limitations, this study develops and evaluates an integrated hydrogeophysical framework that combines AHP-entropy weighting with unsupervised K-means clustering within the DRASTIC model. A comprehensive field survey comprising 30 Vertical Electrical Sounding (VES) stations and 16 high-resolution 2D Electrical Resistivity Tomography (ERT) profiles was conducted across a complex structural transition zone within the southeastern extension of the Niger Delta Basin, Nigeria (covering Itu, Ibiono Ibom, Ikono, and Ini Local Government Areas). The geoelectric models were tightly constrained by local deep borehole lithology logs to differentiate protective clay aquitards from highly transmissive, vulnerable sand units. Substantive framework optimization was achieved using a hybrid Multi-Criteria Decision Analysis and Machine Learning (MCDA-ML) approach, multiplying expert-derived Analytic Hierarchy Process (AHP) weights with objective spatial variance coefficients derived from Shannon's Information Entropy. To establish objective groundwater vulnerability zones, the K-means clustering algorithm was applied to the final continuous DRASTIC vulnerability index scores. Rather than relying on subjective manual thresholding, K-means was utilized to naturally partition the continuous vulnerability index into three distinct categories: low, moderate, and high vulnerability. This clustering was executed on the 30 m × 30 m raster cells encompassing the entire study area. Consequently, the classification provides a continuous spatial vulnerability assessment across the region, rather than being restricted solely to the 30 Vertical Electrical Sounding (VES) station coordinates. This processing was validated using the Elbow Method, Silhouette Coefficient (0.62), Calinski-Harabasz Index (108.03), and Davies-Bouldin Index (0.44). High-vulnerability hotspots were isolated in the southern plain sand corridors where highly porous sand matrices offer negligible contaminant attenuation. Moderate vulnerability constitutes the dominant regional background matrix covering intermediate terrains. Isolated low-vulnerability shields were mapped in the northern sector, geologically sustained by dense, low-permeability clay-rich lenses within the Ameki and Imo Shale Formations. The Impact of the Vadose Zone exhibited the highest mean effective weight in the single-parameter analysis, indicating strong localized influence on the vulnerability index. Depth to Water (with Maximum effective weight of 54.72%), exhibited the highest mean sensitivity in the map-removal analysis, indicating that it was the most influential parameter in the overall index under the adopted weighting scheme. Conversely, Hydraulic Conductivity perfectly stabilized at 0.00% variation across both diagnostic routines (Map Removal Sensitivity Analysis and Single-Parameter Sensitivity Analysis), demonstrating that the hybrid methodology successfully neutralized non-informative spatial parameters. The resulting field-calibrated framework provides a potentially transferable approach for groundwater vulnerability assessment and aquifer protection in heterogeneous sedimentary basins.

✉ Ettiabasi B. Umoren: ettiobongumoren@gmail.com

Department of Physics, Akwa Ibom State University, Mkpat Enin, Akwa Ibom State

Keywords: Groundwater Vulnerability; DRASTIC Index; Electrical Resistivity Tomography; Shannon's Information Entropy; K-Means Clustering; Sensitivity Analysis, Niger Delta

Article history
Received: June 17, 2026
Received in revised form: August 19, 2026
Accepted for publication: August 21, 2026
Available online: August 25, 2026

1.0 Introduction

The assessment of groundwater vulnerability to anthropogenic contamination constitutes a cornerstone of modern hydrogeological resource management, particularly within sub-Saharan Africa's rapidly urbanizing sedimentary basins (Udosen & George, 2018). For decades, index overlay methods, most notably the standard DRASTIC framework established by Aller et al. (1987), have served as important approaches for mapping aquifer vulnerability. However, a critical methodological limitation and technical gap persist at the intersection of classical multi-criteria decision-making frameworks and real-world spatial heterogeneity. Traditional applications of these models rely on fixed, subjective weightings determined by historical Delphi panels or the classic Analytic Hierarchy Process (AHP), which inherently assumes a uniform structural influence of parameters across varying geological terrains (Machiwal et al., 2016; George et al., 2018, 2022a; Uwa et al., 2019). This rigid, deterministic approach overlooks the local variations in data distribution and fails to account for the spatial variance of field parameters, frequently leading to over- or under-estimations of vulnerability along highly sensitive, heterolithic stratigraphic boundaries (George et al., 2014; Ekanem & Ebong, 2026). Recent attempts to optimize index overlay models have integrated subjective AHP with objective statistical weighting tools, such as Shannon's Information Entropy, to capture the intrinsic variance of environmental datasets (Ghazavi & Ebrahimi, 2019; Kazakis & Voudouris, 2017). Yet, these hybrid approaches remain constrained by a second technical limitation: the final vulnerability classification invariably depends on arbitrary, human-defined numerical intervals or slicing techniques (such as equal intervals and natural breaks). This introduces an element of cognitive bias that can obscure natural geochemical and geoelectrical boundaries. The arbitrary discretization of continuous numerical variables fails to reflect the true mathematical distribution of risk within complex transition zones, where permeable unconfined units grade into low-permeability clays.

Although modified DRASTIC models using AHP, entropy weighting and machine learning have increasingly been applied to groundwater vulnerability assessment, important limitations remain in heterogeneous sedimentary environments. In particular, few studies have combined field constrained VES and ERT information with objective entropy weighting and unsupervised clustering to define vulnerability classes without relying solely on predetermined index intervals. The present study therefore evaluates an integrated AHP-entropy-K-means DRASTIC framework for groundwater vulnerability mapping in parts of Akwa Ibom State, Nigeria. The specific objectives are to characterize the subsurface using VES and ERT, derive spatial DRASTIC parameters from the hydrogeophysical and ancillary datasets, determine hybrid parameter weights using AHP and Shannon entropy, identify vulnerability zones using K-means clustering, and evaluate parameter influence using map-removal and single-parameter sensitivity analyses

2.0 Location of the study Area

The study area encompasses approximately 1,240 km² and is bound between latitudes 5°05'N to 5°35'N and longitudes 7°35'E to 8°55'E. Elevation ranges from 33 m in the riverine floodplains of Ini to 137 m in the northern uplands. Major land-use activities are predominantly subsistence agriculture and rapidly expanding peri-urban settlements. Groundwater occurs under unconfined to semi-confined conditions, with depths to the water table ranging from 5.1 m to over 45 m. Active boreholes tap into the regional sands at depth ranges of 60 m to 150 m. Total annual precipitation frequently exceeds 2,500 mm (based on 1990–2020 climatic data from the Nigerian Meteorological Agency).The study area is located within the northeastern corridor of Akwa Ibom State, Nigeria, and is bounded by the administrative limits of the Ibiono Ibom, Itu, Ikono, and Ini Local Government Areas (LGAs) as shown in Figure 1.

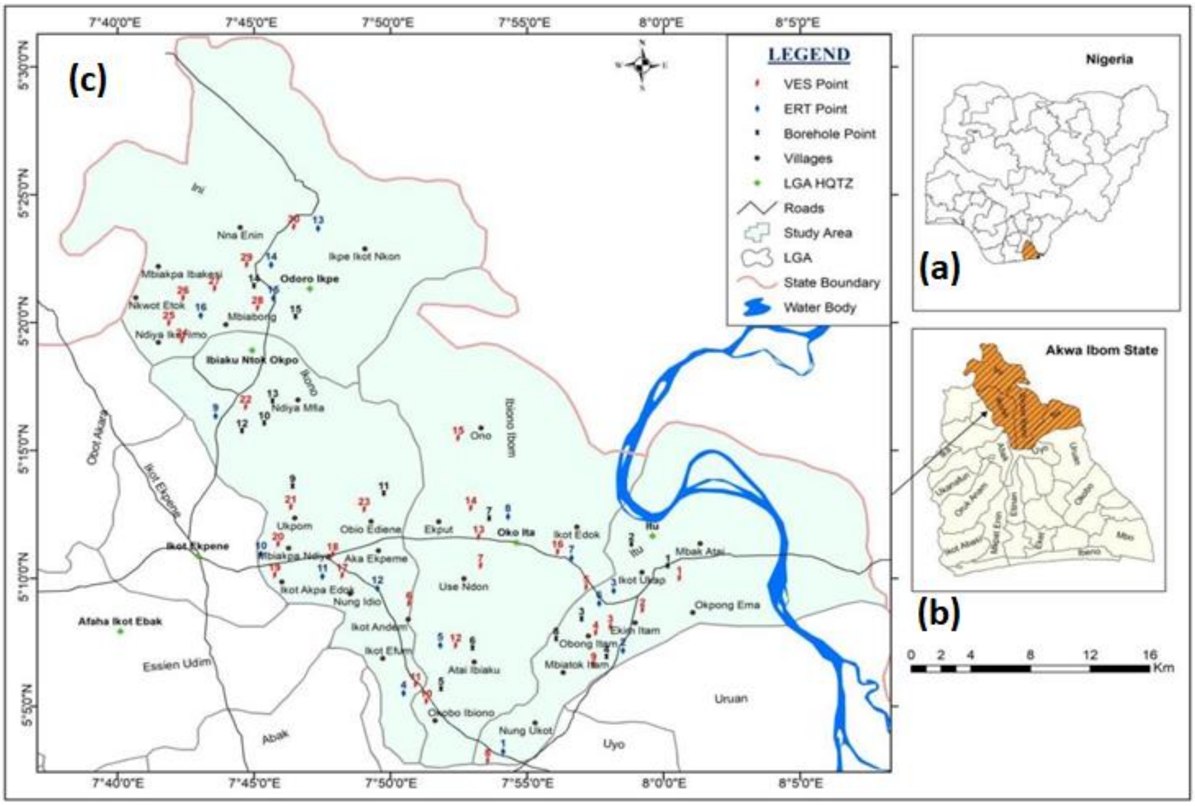

Figure 1: Location map of the study area (a) Nigeria showing study Akwa Ibom state (b) Akwa Ibom state showing study area (c) Study area showing the sounding stations

The terrain lies within the Niger Delta sedimentary basin, characterized by a distinct flat-topped topography with gentle slopes that slope toward the Atlantic coast (Udo & Mode, 2013; George & Thomas, 2023; Inyang et al., 2024a, b; Umoh et al., 2022, 2025). The regional climate is equatorial and humid, featuring an extended rainy season (from April to October) and a shorter dry spell (from November to March) (George et al., 2020, 2021; Ekanem et al., 2024; Udosen et al., 2024a, b, c). Total annual precipitation frequently exceeds 2,500 mm, acting as the primary source of active recharge to the shallow unconfined aquifer systems (George & Thomas, 2024, Udosen et al., 2024d, e).

Geologically, the study area marks a complex structural transition within the southeastern extension of the Niger Delta Basin, showing highly heterogeneous stratigraphy and complex facies variations. The distribution of the various formations depicted in Figure 2, directly governs the regional hydrogeologic framework. The Imo Shale dominates the northern zones of Ibiono Ibom, Ikono, and Ini. This Lower Eocene Formation consists of thick, fissile, impermeable shale beds that restrict vertical fluid flow and form a substantial regional aquitard (Akankpo et al., 2018; George, 2021 a, b; Obianwu et al., 2011; Udo et al., 2023; Udosen et al., 2023; Ekpo et al., 2024).

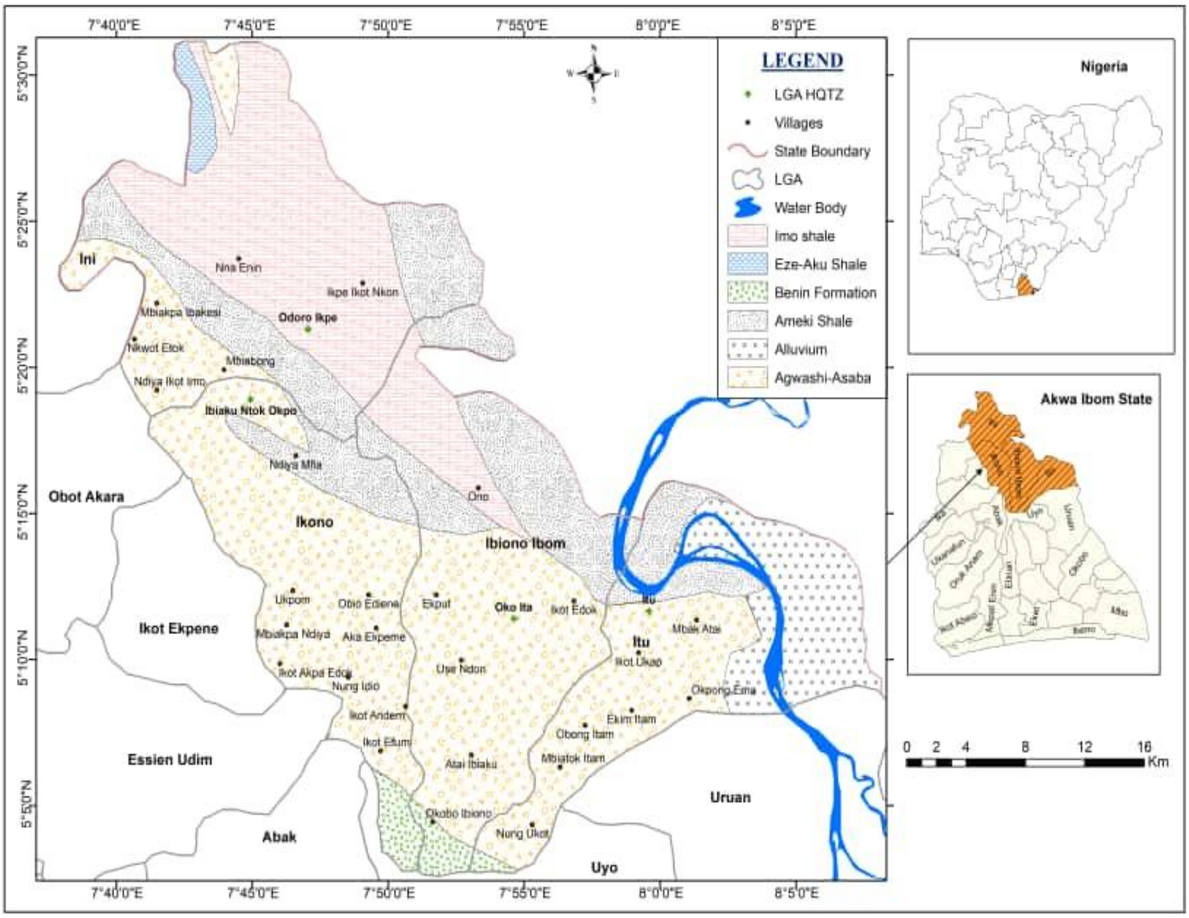

Figure 2: Geologic map of the study area

The Ameki Formation outcrops across the northern margins of Ibiono Ibom and Ini. It features intercalated sandstones, shales, and limestone layers, producing a highly anisotropic aquifer system with variable, fracture-controlled flow regimes (Oki & Akamigbo, 2020). The Ogwashi-Asaba Formation extends across major parts of Itu, Ibiono Ibom, Ikono, and Ini, characterized by alternating sequences of lignite seams, structural clays, and coarse sands. The Benin Formation blankets the southern sectors of Ibiono Ibom and extends into parts of Ikono. This formation consists of highly porous, unconsolidated, continental quartz-sand matrices that offer high groundwater yields but possess very low contaminant attenuation capacities (Ebong et al., 2017; Ekanem, 2022; George et al., 2017, 2022a, b, c). Recent Alluvium deposits are concentrated along the northeastern margins of Itu adjacent to the Cross River flood plain. These deposits consist of highly variable sequences of silt, organic clay, and fine-grained gravelly sands.

3.0 Materials and Method

3.1 1D Vertical Electrical Sounding (VES)

In order to establish a deep, vertical geoelectric stratigraphic framework across the study area, a geophysical survey comprising 30 Vertical Electrical Sounding (VES) stations was conducted. The soundings utilized the classical Schlumberger electrode configuration, deploying an ABEM Terrameter SAS 1000 resistivity meter. To ensure sufficient depth of current penetration for profiling the deepest regional aquifers within both the Coastal Plain Sands and the Ameki Formation, the current electrode half-spacing (AB/2) was progressively expanded from a minimum of 1 m to a maximum of 500 m (corresponding to a total AB current electrode separation of 1000 m). During data acquisition, the potential electrode half-spacing (MN/2) was meticulously adjusted to satisfy the mathematical constraint AB/2 ≥ 5MN/2. Adhering strictly to this ratio ensures that the potential difference measured at the center of the array closely approximates the true potential gradient, thereby satisfying the theoretical assumptions of a dipole field as established by Dobrin and Savit (1988).

The instrument intrinsically measured the subsurface apparent resistance (R_a), defined as the ratio of the potential difference (ΔV) to the injected continuous current (I). To translate these raw resistance values into apparent resistivity (ρ_a), the geometric factor (G), which accounts for the spatial distribution of the electrodes, was applied at each discrete measurement interval. For the Schlumberger array, the apparent resistivity was mathematically derived in equation 1, as:

$$\rho a = \pi \times \left\{ \frac{\left(\frac{AB}{2}\right)^2 - \left(\frac{MN}{2}\right)^2}{MN} \right\} \times R_a \qquad (1)$$

The resulting apparent resistivity values were plotted against the corresponding AB/2 spacings on bi-logarithmic axes (Ikpe et al., 2025). Prior to digital inversion, the raw field curves were subjected to manual smoothing. This critical quality-control step involved the identification and removal of spurious data points (defined as anomalous deviations >10% from the local geoelectric trendline, typically induced by localized telluric noise), standardizing the procedure across all 30 locations. The smoothed data were subsequently inputted into WINRESIST software to extract the first-order geo-electrical parameters (true resistivity and thickness of discrete subsurface layers). To resolve inherent non-uniqueness and the phenomena of equivalence and suppression common in resistivity inversion, the initial master-curve matching was heavily constrained. The algorithm was iteratively calibrated against proximate borehole lithology logs until the root-mean-square (RMS) error of the inverse models was optimized to less than 5 % (Asfahani et al., 2023; Udosen et al., 2024e). This precise correlation ensures that the finalized 1D VES curves represent a highly accurate vertical lithostratigraphic sequence.

3.2 2D Electrical Resistivity Tomography (ERT) Acquisition and Processing

While the 1D VES effectively captured the deep vertical stratigraphy, 2D Electrical Resistivity Tomography (ERT) was deployed to resolve shallow, lateral structural anisotropies and geomorphological transitions across the study area (Ekanem et al., 2021; Thomas et al., 2025; George et al., 2026a, b). A total of 16 high-resolution ERT profiles were executed, evenly distributed to ensure representation of 4 distinct profiles per Local Government Area (LGA). The Wenner electrode array configuration was deliberately selected for these continuous 2D profiles due to its superior signal-to-noise ratio and high sensitivity to vertical variations, making it the optimal geometry for resolving near-surface horizontal structures. Data acquisition along each 100 m profile line commenced with an initial minimum electrode spacing ‘a’ of 5 m. To achieve deeper pseudo-depth levels, the electrode spacing was systematically increased in steps of 5 m (a = 5 m, 10 m, 15 m, …) until the total profile length of 100 m was achieved. This specific spatial configuration was designed to maximize the resolution of the shallow subsurface architecture where anthropogenic contamination pathways are most critical.

All 16 ERT profiles were interpreted independently using RES2DINV interpretation software, and utilized specifically to map the lateral continuity of the vadose zone and identify structural discontinuities, providing the spatial constraints necessary for generating the DRASTIC "I" (Impact of Vadose Zone) layer, and “S” (Soil Media). One of the 2D profiles is shown in Figure 3. The uppermost panel is the measured apparent resistivity pseudo-section, middle panel is the calculated apparent resistivity pseudo-section and the bottommost panel is the inverse model resistivity pseudo-section, showing the resistivity variation (2.01 - 165 Ωm) of the shallow layers

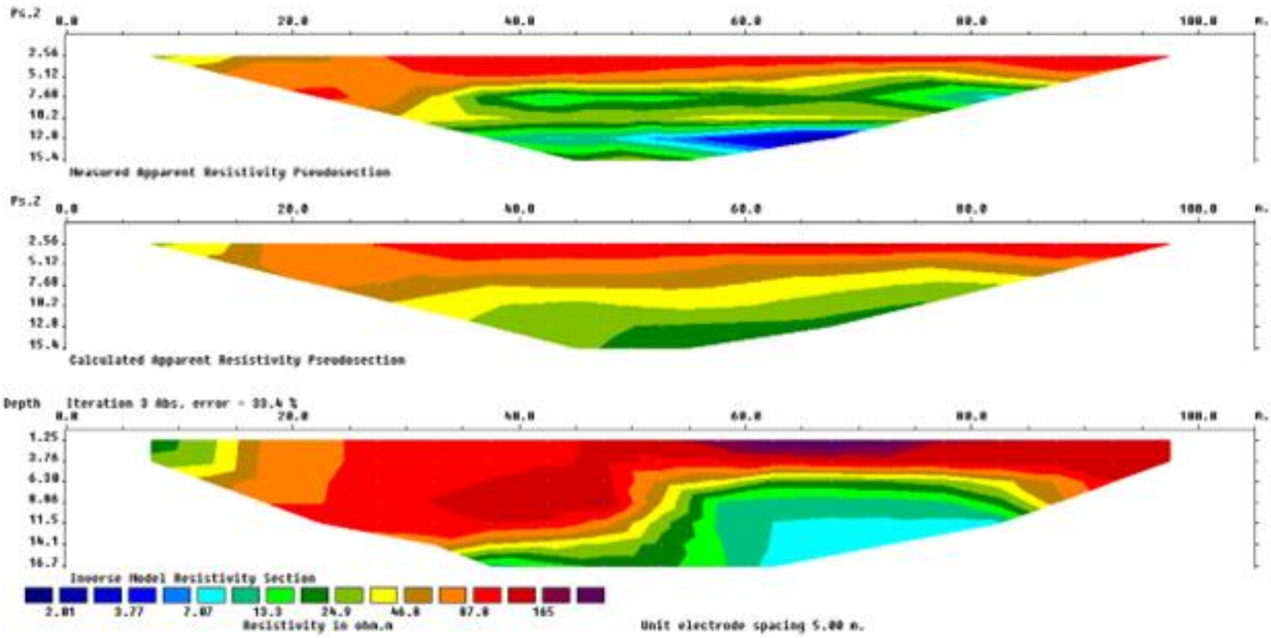

Figure 3: 2D ERT section of the study area

3.3 Correlation of 1D VES Curves and Deep Borehole Logs

Figure 4 represents the correlation of VES curves with near deep borehole lithology data. This correlation is the empirical cornerstone of the hydrogeophysical framework. The borehole information was used to reduce the non-uniqueness associated with geoelectrical inversion and to improve the lithological interpretation of the VES models.”

3.4 Derivation of Modified Geo-Electric DRASTIC Parameters

Research have shown that some of the most important factors that control aquifer pollution potential include net recharge, soil type, depth to water, topography, aquifer material, impact of the unsaturated zone, aquifer media and the hydraulic conductivity, literally termed as DRASTIC parameters. Aller et al. (1987) devised a numerical ranking system to assess aquifer contamination potential in a hydrogeological setting. Here notes are assigned between 1 and 10 and weights between 1 and 5 for each of the DRASTIC parameters. The DRASTIC index (D_I) is calculated using seven weighted environmental parameters shown in equation 2:

$$D_I = D_w D_r + R_w R_r + A_w A_r + S_w S_r + T_w T_r + I_w I_r + C_w C_r \quad (2)$$

where D is depth to water; R is net recharge; A is aquifer media, S is soil media; T is topography; I is impact of vadose zone and C is hydraulic conductivity. The hydrogeophysical parameters calculated for DRASTIC Index were calibrated and scored against the standard seven-index framework established by Aller et al. (1987) to map local variations in vulnerability as presented in Table 1.

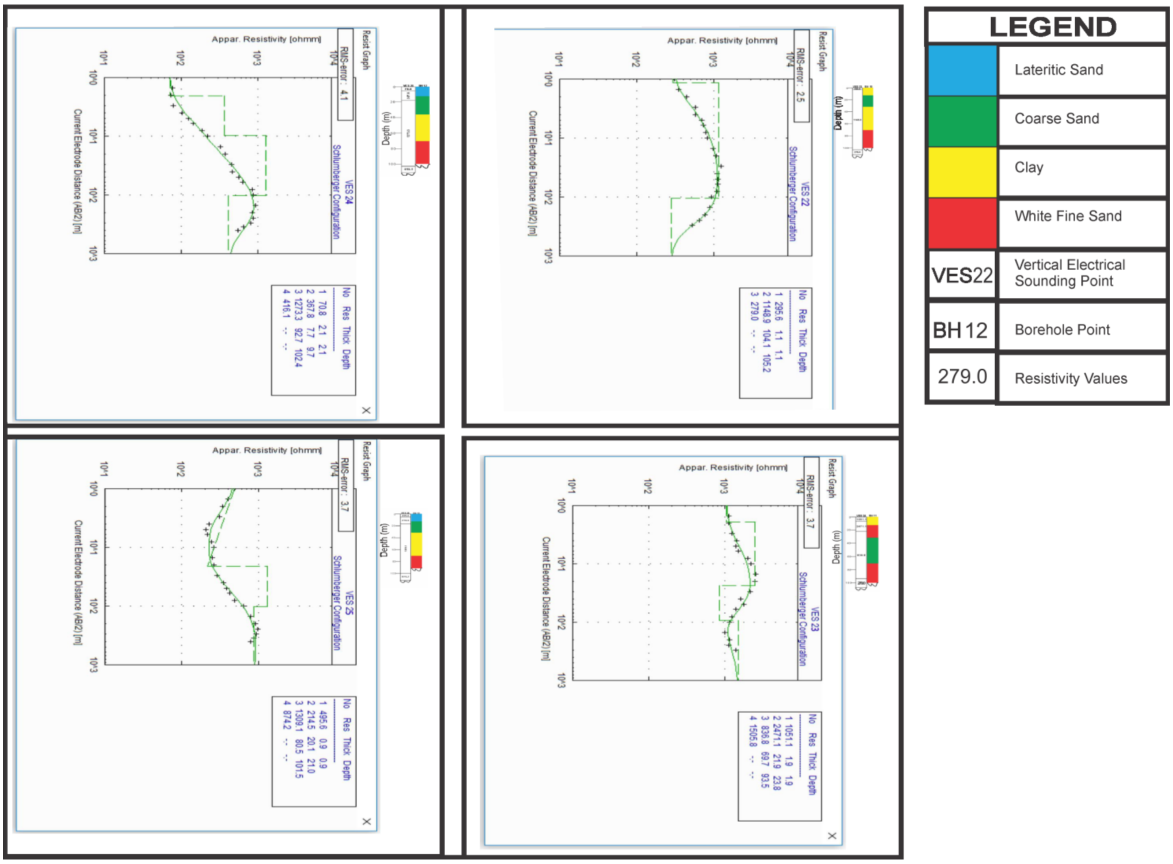

Figure 4: Distribution of deep borehole constrained VES curves in the study area

The final calculated DRASTIC vulnerability indices obtained from equation 2 are assigned classes based on Table 2.

3.4.1 Depth to Groundwater (D)

This parameter reflects the distance a contaminant must travel before reaching the aquifer. It was measured as the vertical distance from the ground surface down to the first continuous geoelectric inflection point indicating water saturation. This was identified via an inversion drop in resistivity from the geoelectric boundary. These values were continuously calibrated against static water level (SWL) measurements obtained from active local boreholes.

3.4.2 Net Recharge (R)

Rainfall constitutes the primary source of groundwater recharge in the study area. In the absence of direct net recharge data, the formulation by Piscopo (2001), later adopted by Ekanem et al. (2024a); was utilized to compute the net recharge index (R) according to Equation 3:

$$NET\ RECHARGE = SF + RF + SPF \quad (3)$$

where SF is the slope factor, RF is the rainfall factor (in mm) and SPF is the soil permeability factor. The average annual rainfall in the study area according to Isaiah et al. (2021) is about 2007.9 mm. The slope (in %) for the study area was obtained from the ASTER digital elevation model (DEM), through the use of ArcGIS 10.5. The soil permeability K_p required to estimate the net recharge values were determined via the use of equation 4 as:

$$K_p = \frac{C\mu_d}{\delta_w g} \quad (4)$$

where C is the estimated hydraulic conductivity based on equation 5, δ_w is water density (1000 kg/m^3), g is the acceleration due to gravity (9.8m/s^2) and μ_d is the dynamic viscosity of water which was taken as 0.0014 kg/ms according to Fetter (1994).

Table 1: Ranges, ratings and weight of DRASTIC factors (Aller et al., 1987)

Depth of water (m)			Aquifer media			Soil Media			Topography			Impact of vadose zone			Hydraulic conductivity (m/s)		
Interval	**R**	**W**	**Interval**	**R**	**W**	**Interval**	**R**	**W**	**Interval**	**R**	**W**	**Interval**	**R**	**W**	**Interval**	**R**	**W**
< 20	10	5	Massive Shale	2	3	Thin or absent	10	2	0 – 5	10	1	Thin or absent	10	5	> 9.4×10^{-4}	10	3
20 - 40	9		Metamorphic/Igneous	3		Gravel	10		5 – 15	8		Gravel	10		$4.7x10^{-4}$ – $9.4x10\text{-}^{4}$	8	
40 - 60	7		Weathered	4		Sand	9		15 – 25	6		Sand	9		$32.9x10^{-5}$- $4.7x10^{-4}$	6	
60 - 80	5		Glacial Till	5		Laterite/Peat	8		25 – 35	4		Laterite/Peat	8		$14.7x10^{-5}$-$32.9x10^{-5}$	4	
80 - 100	3		Bedded Sandstone	6		Shrinking/Aggregated Clay	7		> 35	1		Shrinking sand/Aggregated Clay	7		$4.7x10^{-5}$-$14.7x10^{-5}$	2	
100 - 120	2		Limestone and Shale	6		Sandy Loam	6					Sandy Loam	6				
> 120	1		Sequences	6		Loam	5					Loam	5		$4.7x10^{-7}$-$4.7x10^{-5}$	1	
			Massive Sandstone	6		Silty Loam	4					Silty Loam	4				
			Massive Limestone	6		Clay Loam	3					Clay Loam	3				
			Sand and gravel	8		Muck	2					Muck	2				
			Basalt	9		Non-Shrinky and non-aggregated clay	1					Non-Shrinky and non-aggregated clay	1				
			Karst Limestone	10													

This parameter is assigned weight of 4, and rating from 1 to 10 according to Table 3.

3.4.3 Aquifer Media (A)

This parameter evaluates the attenuation capacity of the geological formation housing the aquifer. For this study, the aquifer media classifications were derived directly from geological borehole lithological logs, which were spatially constrained by Vertical Electrical Sounding (VES) interpretations. The weighting of aquifer media was done according to the data in Table 1.

3.4.4 Soil Media (S)

Soil media was determined from the structural properties of the first geoelectric layer topsoil from the VES interpretation, constrained with 16 ERT cross-sections, in correlation with the geological borehole logs. The weighting of soil media for this study was assigned according to Table 1.

3.4.5 Topography (T)

Topography refers to the slope of the earth (land) surface. The slope (in %) for this study, was extracted from digital elevation models (DEM) and ground-truthed at each of the 30 VES points using GPS altimetry data. Ratings assigned for topography from 1 to 10 according to Table 1.

3.4.6 Impact of the Vadose Zone (I)

Impact of vadose zone was determined by analyzing the composition and thickness of the unsaturated layer overlying the aquifer as obtained from the from the geological borehole logs constrained VES curves. Weight and ratings were assigned according to Table 1.

3.4.7 Hydraulic Conductivity (C)

Hydraulic conductivity dictates the flow rate of groundwater, thereby determining the speed at which a contaminant disperses through the aquifer. For this study, hydraulic conductivity (C) was empirically estimated using Archie's law-based approach from the bulk resistivity of the soil layer (ρ), and assumed regional porosity values, measured in m/day, utilizing Equation 5. The weight of this parameter is 3, and the parameter values were assigned ratings from 1 to 10 based on Table 1.

$$C = 139.12{\rho_b}^{-0.728} \qquad (5)$$

where ρ_b is soil layer bulk resistivity. The summary of the source, processing and resolution of the DRASTIC parameters is presented in Table 4. The computed DRASTIC Index result summary is presented in Table 5.

Table 2: DRASTIC Index and Vulnerability class (modified from Aller et al., 1987, Amini et al., 2020)

DRASTIC Index (DI)	Vulnerability Class
1-100	Low
101-175	Moderate
176-200	High
>200	Very High

Table 3: Net Recharge ratings for the study (Piscopo, 2001; Al-Adamant et al., 2003)

Slope (%)	Rating	Rainfall (mm)	Rating	Soil permeability	Rating	Net recharge (weight W = 4)	Rating
< 2	4	< 500	1	Very slow	1	11 – 13	10
2 – 10	3	500 – 700	2	Slow	2	9 – 11	8
10 – 33	2	700 – 850	3	Moderate	3	7 – 9	5
> 33	1	> 850	4	Mod – high	4	5 -7	3
				High	5	3 - 5	1

Table 4: DRASTIC Parameter sources, resolution, and processing

Parameter	Data source	Original resolution	Processing	Final resolution (m)
D	VES/boreholes	...	Interpolation	30 m
R	rainfall/recharge data	...	Recharge model	30 m
A	VES/ERT/geology	...	Lithological classification	30 m
S	soil map	...	Rating	30 m
T	DEM	...	Slope calculation	30 m
I	VES/ERT	...	Vadose zone lithology	30 m
C	hydraulic data/empirical relation	...	Empirical conversion	30 m

3.5 Step-by-Step approach in Hybridizing ML-MCDA

3.5.1 Spatial Data Preparation

The standard DRASTIC model, developed by Aller et al. (1987) for the US EPA, relies on fixed structural weights. While this model is reliable, these original weights fail to account for local hydrogeological variances, and classifying the final map into zones using arbitrary index ranges introduces human bias. By upgrading to a hybrid framework, combining the Analytic Hierarchy Process (AHP) for structured expert judgment, Information Entropy for data-driven variation, and Unsupervised K-Means Clustering for automated zonation, we eliminate these structural flaws and produce a statistically defensive vulnerability assessment.

All seven DRASTIC thematic layers; Depth to water table (D), Net Recharge (R), Aquifer media (A), Soil media (S), Topography (T), Impact of vadose zone (I), and Hydraulic conductivity (C), were standardized to a uniform spatial grid resolution (30 m x 30 m) and projected onto a common spatial reference system. Hydrogeological parameter values were converted into standardized ratings ($r_{ij} \in [1, 10]$) following the criteria established by Aller et al. (1987). When a parameter exhibits zero spatial variance across the study domain; such as a uniform hydraulic conductivity rating ($r_{i,C} = k$ for all cells $i = 1, 2\ldots, n$), it functions as a static background baseline. To prevent mathematical singularity and numerical instabilities in subsequent statistical transformations, the constant parameter C was retained during subjective expert evaluation (AHP) but flagged and isolated prior to objective entropy normalization.

3.5.2 Subjective Weight Allocation via Analytic Hierarchy Process (AHP)

To objectively determine the relative importance of the DRASTIC hydrogeological parameters for groundwater vulnerability assessment, the Analytic Hierarchy Process (AHP) was employed. A pairwise comparison matrix was constructed using Saaty's 1 – 9 fundamental scale, allowing for the systematic evaluation of each parameter's influence on aquifer contamination potential (Table 1). Depth to Water (D) and Impact of Vadose Zone (I) were assigned the highest comparative importance due to their primary roles in regulating pollutant attenuation and transport time, whereas Topography (T) was assigned the lowest.

Because standard DRASTIC parameters possess varying degrees of influence on aquifer contamination, we established the matrix using Thomas Saaty's 1 – 9 scale to reflect the traditional relative importance of each parameter (where D and I are most critical, and T is least).

Table 5: Traditional DRASTIC Index Vulnerability result

VES NO	Parameter	D		R		Ar		S		T		I		C		DI values	Vulnerability rating
	Weight		5		4		3		2		1		5		3		
	Location	D_r	D_rD_W	R_r	R_rR_W	A_r	A_rA_W	S_r	S_rS_W	T_r	T_rT_W	I_r	I_rI_W	C_r	C_rC_W		
1	Mbak Atai, Itu	3	15	10	40	4	12	1	2	10	10	10	50	1	3	132	Moderate
2	Okpong Ema Itam, Itu	5	25	8	32	8	24	3	6	10	10	10	50	1	3	150	Moderate
3	Ekim Itam, Itu	9	45	5	20	4	12	3	6	6	6	1	5	1	3	97	Low
4	Obong Itam, Itu	3	15	8	32	6	18	3	6	10	10	10	50	1	3	134	Moderate
5	Ikot Ukap, Itu	3	15	8	32	6	18	6	12	10	10	10	50	1	3	140	Moderate
6	Ikot Andem Itam, Itu	5	25	5	20	4	12	10	20	10	10	3	15	1	3	105	Moderate
7	Use Ndon, Ibiono Ibom	5	25	8	32	3	9	6	12	10	10	9	45	1	3	136	Moderate
8	Nung Ukot Itam, Itu	3	15	8	32	6	18	3	6	10	10	3	15	1	3	99	Low
9	Mbiatok Itam, Itu	2	10	8	32	4	12	3	6	10	10	10	50	1	3	123	Moderate
10	Okobo, Ibiono Ibom	2	10	8	32	4	12	6	12	10	10	10	50	1	3	129	Moderate
11	Ikot Efum, Ibiono Ibom	5	25	3	12	4	12	10	20	8	8	10	50	1	3	130	Moderate
12	Atai Ibiaku, Ibiono Ibom	3	15	8	32	6	18	3	6	10	10	9	45	1	3	129	Moderate
13	Okoita, Ibiono Ibom	3	15	5	20	4	12	6	12	8	8	10	50	1	3	120	Moderate
14	Ekput, Ibiono Ibom	1	5	5	20	4	12	6	12	10	10	10	50	1	3	112	Moderate
15	Ono, Ibiono Ibom	2	10	5	20	6	18	9	18	6	6	10	50	1	3	125	Moderate

16	Ikot Edok, Ibiono Ibom	1	5	8	32	3	9	6	12	10	10	9	45	1	3	116	Moderate
17	Nung Idio, Ikono	3	15	8	32	4	12	3	6	8	8	10	50	1	3	126	Moderate
18	Aka Ekpeme, Ikono	5	25	5	20	4	12	6	12	10	10	1	5	1	3	87	Low
19	Ikot Akpadok Ndiya, ikono	5	25	8	32	4	12	3	6	8	8	1	5	1	3	91	Low
20	Mbiakpan Ndiya, ikono	3	15	8	32	4	12	6	12	8	8	10	50	1	3	132	Moderate
21	Ukwongho Ukpom, Ikono	3	15	8	32	3	9	6	12	8	8	9	45	1	3	124	Moderate
22	Ndiya Mfia, Ikono	2	10	8	32	3	9	3	6	10	10	9	45	1	3	115	Moderate
23	Obio Ediene, Ikono	3	15	8	32	6	18	9	18	8	8	8	40	1	3	134	Moderate
24	Ndiya Ikotimo, Ini	2	10	8	32	4	12	1	2	8	8	9	45	1	3	112	Moderate
25	Mbiabong Ikpe, Ini	2	10	8	32	4	12	6	12	10	10	9	45	1	3	124	Moderate
26	Ukwot Etok, Ini	1	5	8	32	4	12	3	6	10	10	3	15	1	3	83	Low
27	Mbiakpa Ibakesi, Ini	5	25	8	32	4	12	9	18	10	10	10	50	1	3	150	Moderate
28	Odoro Ikpe, Ini	3	15	8	32	4	12	9	18	10	10	9	45	1	3	135	Moderate
29	Nna Enin Ikpe, Ini	3	15	8	32	4	12	3	6	10	10	10	50	1	3	128	Moderate
30	Ikpe Ikot Nkon	3	15	8	32	4	12	3	6	10	10	3	15	1	3	93	Low

Step-by-step mathematical workflow:

Step 1: Creation of Pairwise Comparison Matrix

By comparing every parameter against every other parameter. An assignment of 1 means equal importance, while higher numbers (such as 5) indicate strong importance. The inverse (example, 1/5 or 0.20) is automatically assigned for the reverse comparison as shown in Table 6.

Step 2: Normalizing the Matrix

Subjective criteria weights (w_j^A) were derived using the standard Analytic Hierarchy Process (Saaty, 1980). A pairwise comparison matrix A = $[a_{jk}]_{m\times m}$ (where m = 7) was constructed using Saaty's 1 – 9 fundamental scale. The subjective weight vector $w^A = [w_1^A, w_2^A, \ldots, w_m^A]^T$ was determined by solving the principal eigenvalue problem according to Equation 5:

$$Aw^A = \lambda_{max} w^A \quad (5)$$

subject to the normalization constraint in equation 6:

$$\sum_{i=1}^{m} w_j^A = 1 \quad (6)$$

To make the scores comparable, we divided each cell by its respective Column Sum from as presented in Table 7.

Step 3: Calculation of the Final Eigenvector (Weights)

We find the final weight for each parameter by calculating the mean average of its row in the normalized matrix as shown in table 8.

Table 6: Pairwise Comparison Matrix

Parameter	D	R	A	S	T	I	C
D	1.00	1.00	2.00	2.00	5.00	1.00	2.00
R	1.00	1.00	1.00	2.00	4.00	1.00	1.00
A	0.50	1.00	1.00	2.00	3.00	0.50	1.00
S	0.50	0.50	0.50	1.00	2.00	0.50	0.50
T	0.20	0.25	0.33	0.50	1.00	0.20	0.33
I	1.00	1.00	2.00	2.00	5.00	1.00	2.00
C	0.50	1.00	1.00	2.00	3.00	0.50	1.00
Column Sum	4.70	5.75	7.83	11.50	23.00	4.70	7.83

Table 7: Normalized Pairwise Matrix Result

Parameter	D	R	A	S	T	I	C
D	0.2128	0.1739	0.2554	0.1739	0.2174	0.2128	0.2554
R	0.2128	0.1739	0.1277	0.1739	0.1739	0.2128	0.1277
A	0.1064	0.1739	0.1277	0.1739	0.1304	0.1064	0.1277
S	0.1064	0.0870	0.0639	0.0870	0.0870	0.1064	0.0639
T	0.0426	0.0435	0.0421	0.0435	0.0435	0.0426	0.0421
I	0.2128	0.1739	0.2554	0.1739	0.2174	0.2128	0.2554
C	0.1064	0.1739	0.1277	0.1739	0.1304	0.1064	0.1277

Table 8: Final Eigenvector (Weights)

Parameter	Final Weight (Decimal)	Final Weight (%)
Depth to Water (D)	0.2145	21.45
Impact of Vadose Zone (I)	0.2145	21.45
Net Recharge (R)	0.1718	17.18
Aquifer Media (A)	0.1352	13.52
Hydraulic Conductivity (C)	0.1352	13.52
Soil Media (S)	0.0859	8.59
Topography (T)	0.0429	4.29
Total	1.0000	100.00

Step 4: Consistency Check

To ensure the logical validity of the judgments:

1. Calculate λ_{max} (Principal Eigenvalue): Multiply the initial column sums by the final weights, then sum the results as shown in Equation 7.

$$\lambda_{max} = (4.70 \times 0.2145) + (5.75 \times 0.1718) + \ldots (7.83 \times 0.1352) = 7.0927 \quad (7)$$

2. Calculate Consistency Index (CI): For n = 7 parameters using Equation 8:

$$CI = \frac{\lambda_{max} - m}{m-1} = x = \frac{7.0927 - 7}{6} = 0.0154 \quad (7)$$

3. Calculate Consistency Ratio (CR): We divide CI by the Random Index (RI). For n = 7, Saaty's standard RI is 1.32 according to Equation 9.

$$CR = \frac{CI}{RI} = \frac{0.0154}{1.32} = 0.0117 \quad (9)$$

Because CR = 0.0117, which is significantly less than the standard threshold of 0.10, the matrix is statistically consistent, and the resulting weights are mathematically valid for modeling. The Pairwise Comparison Matrix and resulting Weights for the DRASTIC Parameters are given in Table 9.

Table 9: Pairwise Comparison Matrix and Resulting Weights for DRASTIC Parameters

Parameter	D	R	A	S	T	I	C	Final Weight
Depth to Water (D)	1.00	1.00	2.00	2.00	5.00	1.00	2.00	0.2145
Net Recharge (R)	1.00	1.00	1.00	2.00	4.00	1.00	1.00	0.1718
Aquifer Media (A)	0.50	1.00	1.00	2.00	3.00	0.50	1.00	0.1352
Soil Media (S)	0.50	0.50	0.50	1.00	2.00	0.50	0.50	0.0859
Topography (T)	0.20	0.25	0.33	0.50	1.00	0.20	0.33	0.0429
Impact of Vadose Zone (I)	1.00	1.00	2.00	2.00	5.00	1.00	2.00	0.2145
Hydraulic Cond. (C)	0.50	1.00	1.00	2.00	3.00	0.50	1.00	0.1352

The subjective weight w_C^A remains non-zero, preserving the recognized hydrogeological importance of hydraulic conductivity within expert assessment.

3.5.3 Objective Weight Derivation via Shannon Entropy

To objectively quantify the spatial information content imparted by each parameter layer, Shannon's Entropy model (Shannon, 1948) was applied.

Step one: The normalized value P_{ij} for parameter *j* at spatial location *i* was calculated using Equation 10:

$$P_{ij} = \frac{P_{ij}}{\sum_{i=1}^{n} r_{ij}} \quad (10)$$

Each location's rating for parameter was divided by the sum of all ratings for that parameter.

Step two: The normalized informational entropy E_j associated with the *j*-th parameter was derived via Equation 11:

$$E_j = -\frac{1}{\ln(n)} \sum_{i=1}^{n} p_{ij} \ln(p_{ij}) \qquad (11)$$

where n represents the total number of spatial grid cells.

Step three: The degree of spatial divergence (d_j) was calculated using Equation 12:

$$d_j = 1 - E_j \qquad (12)$$

Step four: The resulting objective weight (w_j^E) was calculated by Equation 13:

$$w_j^E = \frac{d_j}{\sum_{k=1}^{m} d_k} \qquad (13)$$

For a zero-variance layer such as C, the uniform probability distribution ($P_{i,C} = \frac{1}{n}$) yields maximum entropy (E_C = 1.0) and zero divergence (d_C= 0). Consequently, the objective entropy weight naturally evaluates to w_C^E = 0, automatically nullifying the parameter's contribution to objective spatial dispersion.

3.5.4 Hybrid Weight Integration Schemes

To synthesize subjective expert judgments (W_j^A) with objective information entropy (w_j^E), integrated weights (W_j) were calculated. At this point, Multiplicative Hybridization (Strict Variance Filtering) was evaluated via the use of Equation 14:

$$\alpha_j = W_j^A . w_j^E \Rightarrow W_j = \frac{\alpha_j}{\sum_{k=1}^{m} \alpha_k} \qquad (14)$$

Under this formulation, W_C = 0, effectively filtering out zero-variance layers from the composite vulnerability score.

By applying Shannon Entropy, the calculation measures the variance and distribution of scores across the study area. Because the Hydraulic Conductivity (C) parameter is completely constant (scored as 3) across all 30 points in this dataset, it carries a maximum entropy value of exactly 1.0. Consequently, its divergence is zero. In Shannon's information theory, a constant parameter provides no new comparative information or spatial variance to differentiate vulnerability across the site, resulting in an objective weight (and subsequently a hybrid weight) of zero. The normalized entropy values obtained is presented in Table 10.

Table 10: Objective Entropy and Hybrid AHP-ENTROPY Weights based on 30 VES Points

Parameter	Normalized Entropy (E_j)	Divergence (d_j)	Objective Weight ($W_{entropy}$)	AHP Weight (W_{ahp})	Hybrid Weight (W_{hybrid})
Depth to Water (D)	0.9662	0.0338	0.2706	0.2145	0.3570
Net Recharge (R)	0.9930	0.0070	0.0564	0.1718	0.0596
Aquifer Media (A)	0.9908	0.0092	0.0733	0.1352	0.0610
Soil Media (S)	0.9612	0.0388	0.3104	0.0859	0.1640
Topography (T)	0.9972	0.0028	0.0222	0.0429	0.0059
Impact of Vadose Zone (I)	0.9666	0.0334	0.2671	0.2145	0.3525
Hydraulic Conductivity (C)	1.0000	0.0000	0.0000	0.1352	0.0000
Total	-	-	1.0000	1.0000	1.0000

3.5.5 DRASTIC Vulnerability Index (DVI) Mapping

The continuous spatially distributed DRASTIC Vulnerability Index (DVI_i) was computed for each grid cell *i* through weighted linear combination as in Equation 15:

$$DVI_i = \sum_{j=1}^{m} W_j . r_{ij} \qquad (15)$$

Because $r_{i,C}$ is spatially invariant, its contribution in the additive model functions as a uniform scalar translation across the spatial field, leaving the relative spatial gradient driven by D, R, A, S, T, and I unaltered.

3.5.6 Unsupervised K-Means Spatial Clustering and Zoning

To establish objective groundwater vulnerability zones, the K-means clustering algorithm was applied to the final continuous DRASTIC vulnerability index scores. Rather than relying on subjective manual thresholding, K-means was utilized to naturally partition the continuous vulnerability index into three distinct categories: low, moderate, and high vulnerability. This clustering was executed on the 30 m × 30 m raster cells encompassing the entire study area. Consequently, the classification provides a continuous spatial vulnerability assessment across the region, rather than being restricted solely to the 30 Vertical Electrical Sounding (VES) station coordinates.

Before computing the final vulnerability index, zero-variance layers (C) were explicitly removed from the dataset to avoid division-by-zero errors during Z-score standardization of the individual parameters, using equation 16:

$$z_{ij} = \frac{x_{ij} - \mu_j}{\sigma_j} \qquad (16)$$

where μ_j and σ_j denote the spatial mean and standard deviation of parameter j, respectively.

Once the final continuous DRASTIC vulnerability index was computed, these final scalar scores were clustered by minimizing the total within-cluster sum of squares (J) according to equation 17:

$$J = \sum_{i=1}^{k} \sum_{x \epsilon C_i} \|x - \mu_i\|^2 \qquad (17)$$

where μ_k represents the centroid vector of cluster C_k. The optimal number of vulnerability zones was determined using Silhouette analysis and the Elbow method. The algorithm minimizes the within-cluster sum of squares (WCSS) to automatically group the continuous index pixels into discrete, statistically homogenous vulnerability zones.

3.6 Cluster Optimization and Validation

3.6.1 The Elbow Plot Method

A recurring limitation in environmental vulnerability mapping is the subjective classification of continuous index scores into discrete hazard zones using arbitrary equal intervals or manual geometric breaks (Motlagh et al., 2023). To eliminate subjectivity in partitioning the computed Hybrid AHP-Entropy DRASTIC Vulnerability Index into distinct risk zones, an unsupervised machine learning approach via k-means clustering was deployed (Uzcategui-Salazar, & Lillo, 2025). The determination of the optimal number of vulnerability clusters k was mathematically formalized utilizing the Elbow Method, a cluster-validation technique originally conceptually proposed by Thorndike (1953) and expanded across multivariate datasets by Kaufman and Rousseeuw (1990). The Within-Cluster Sum of Squares (WCSS), or cluster inertia, was evaluated across a spectrum of k values ranging from 1 to 8. WCSS serves as a metric for internal cluster variance and is defined according to (Hastie et al., 2009; Jain, 2010) given in equation 18 as:

$$WCSS = \sum_{i=1}^{k} \sum_{x \epsilon C_i} \|x - \mu_i\|^2 \qquad (18)$$

where C_i represents the ith cluster, x is the vulnerability index vector assigned to that cluster, and μ_i is the centroid of C_i.

3.6.2 K-Means Internal Cluster Validation Metrics

To verify the structural integrity, compactness, and separation of the derived K-means vulnerability zones, three distinct internal validation criteria were computed: the Silhouette Coefficient (Rousseeuw, 1987), the Calinski-Harabasz (C-H) Index (Caliński and Harabasz, 1974), and the Davies-Bouldin (D-B) Index (Davies and Bouldin, 1979).

3.7 Sensitivity Analysis

3.7.1 Map Removal Method

The traditional DRASTIC framework assumes that adding all seven layers provides the most accurate picture of vulnerability. However, in many study areas, certain layers might be redundant, highly correlated, or carry data tracking errors that distort the final map. The Map Removal Sensitivity Analysis (originally developed by Lodwick et al., 1990, and popularized for DRASTIC by Babiker et al., 2005) systematically removes one parameter layer at a time from the DRASTIC index calculation. By measuring how much the index shifts after a layer is removed, the analysis calculates the true, empirical influence of that layer. The sensitivity measure *S* for each of the 30 VES points was calculated using Equation 19.

$$S = \frac{\left|\frac{V}{N} - \frac{V'}{n}\right|}{V} \times 100 \quad (19)$$

where V is the original, unperturbed Hybrid DRASTIC Vulnerability Index calculated using all 7 parameters, V' is the perturbed Vulnerability Index calculated using only 6 parameters (with one layer removed), N is number of layers used to calculate V (N = 7) and n is the number of layers used to calculate V' (n = 6). Division by N and n converts both indices into a normalized per-layer average score before calculating the percentage change.

3.7.2 Single Parameter Method

To perform a Single-Parameter Sensitivity Analysis (Napolitano and Fabbri, 1996), the effective or real weight of each parameter layer at each specific observation point was evaluated. The traditional DRASTIC framework assigns a fixed, constant weight to a parameter across the entire map. However, in reality, the actual influence of a parameter changes from one site to another depending on the local data variations (George et al., 2026 a). The single-parameter sensitivity analysis calculates this point-by-point variation using the following formula in Equation 20.

$$W_{eff} = \frac{W_h - R_i}{DI} \times 100 \quad (20)$$

where W_{eff} is the effective weight of the individual parameter at the VES location (%), W_h is the assigned structural hybrid weight of that parameter, R_i is the empirical value scored at the VES location and DI is the final DRASTIC vulnerability index calculated for the location.

4.4 Results and Discussions

4.1 1D VES Results Interpretation

Table 11 is the result from the interpretation of the 30 Vertical Electrical Sounding (VES) stations across the study area. The interpretation reveals a multi-layered subsurface framework consisting predominantly of 3-to-5 geoelectric layers. The interpreted geoelectric models illuminate significant variations in layer resistivity, thickness, and depth, reflecting the typical lithological heterogeneity of the Niger Delta's Benin Formation and its transition zones.

4.2 Geoelectrical and Lithological Stratigraphy by local government

4.2.1 Itu Local Government Area

The sounding points within Itu LGA (VES 1 to 6, 8, and 9) generally exhibit high-resistivity signatures in the deeper subsurface horizons.

Surficial Layers: Topsoil and shallow layers vary from topographically high sandy clays (example VES 4 with a resistivity of 186.2 Ωm at 104 m elevation) to dry, highly resistive sands like those at VES 6 (2109.7 Ωm).

Aquifer Horizons: Prolific, highly resistive coarse-to-gravelly sand units dominate the second and third layers. For instance, VES 1 (Mbak Atai) and VES 4 (Obong Itam) reveal massive gravelly sand bodies boasting resistivities of 2612.4 Ω.m and 2608.9 Ω.m respectively, terminating in fine-to-coarse sand configurations at depths exceeding 80 meters.

Protective Cover: The presence of a shallow clay unit at VES 1 (85.6 Ωm) and deeper clay units at VES 2 (65.3 Ωm at a depth of 77.8 m) indicates localized clay intercalations within an otherwise sandy aquifer matrix.

Table 11: Summary of VES Interpretation results

VES NO	VES Location	Long. (°)	Lat. (°)	Elevation (m)	Layer number	Resistivity (Ωm)	Thickness (m)	Layer Dep(m)	Lithology
1	Mbak Atai, Itu	5.1721	7.998	97	1	85.6	5.1	5.1	Clay
					2	2612.4	83.2	88.3	Gravelly sand
					3	674.5			Fine Sand
2	Okpong Ema Itam, Itu	5.1444	7.9838	102	1	380.9	0.6	0.6	Clayey Sand
					2	1053.1	28.9	29.6	Coarse Sand
					3	2488.1	48.3	77.8	Gravelly Sand
					4	65.3			Clay
3	Ekim Itam, Itu	5.1337	7.9645	82	1	301.1	0.9	0.9	Clayey Sand
					2	81.2	20.4	21.2	Clay
					3	627.1	72.4	93.6	Fine Sand
					4	126.0			Sandy clay
4	Obong Itam, Itu	5.138	7.9563	104	1	186.2	2.8	2.8	Sandy clay
					2	767.2	15.9	18.7	Fine Sand
					3	2608.9	70	88.7	Gravelly sand
					4	1120.5			Coarse Sand
5	Ikot Ukap, Itu	5.158	7.9542	76	1	991.3	2.0	2.0	Fine Sand
					2	2407.6	97.5	99.4	Gravelly Sand
					3	1628.1			Coarse Sand
6	Ikot Andem Itam, Itu	5.1488	7.8431	78	1	2109.7	1.7	1.7	Gravelly sand
					2	241.1	72.5	74.1	Clayey Sand
					3	845.0			Fine Sand
7	Use Ndon, Ibiono	5.1784	7.8856	114	1	686.2	0.7	0.7	Fine Sand
					2	273.5	6.1	6.8	Clayey Sand
					3	1807.6	64.7	71.4	Coarse Sand
					4	239.1			Clayey Sand
8	Nung Ukot Itam, Itu	5.0474	7.8906	76	1	147.4	0.9	0.9	Sandy clay
					2	1873	11.2	12.1	Coarse Sand
					3	296.0	69.9	82	Clayey Sand
					4	1669.3			Coarse Sand
9	Mbiatok Itam, Itu	5.1148	7.9593	99	1	335.5	1.7	1.7	Clayey Sand
					2	1318.4	28.5	30.2	Coarse Sand
					3	2253.6	84.1	114.3	Gravelly sand
					4	696.2			Fine Sand
10	Okobo, ibiono	5.0854	7.8535	78	1	442.6	3.5	3.5	Fine Sand
					2	1280.2	7.5	11	Coarse Sand
					3	3070.7	89.9	100.9	Gravelly sand
					4	818.3			Fine Sand

11	Ikot Efum, Ibiono	5.0963	7.8471	85	1	2207.0	0.7	0.7	Gravelly sand
					2	403.6	5.4	6.1	Fine Sand
					3	2801.5	72.3	78.4	Gravelly sand
					4	424.9			Fine Sand
12	Atai Ibiaku, Ibiono	5.1215	7.8713	90	1	389.0	4.8	4.8	Clayey Sand
					2	1310.1	92.1	96.8	Coarse Sand
					3	1609.2			Gravelly sand
13	Okoita, Ibiono	5.1916	7.8851	90	1	452.6	1.9	1.9	Fine Sand
					2	2394.9	86.8	88.7	Gravelly sand
					3	429.0			Fine Sand
14	Ekput, Ibiono	5.2029	7.8863	90	1	575.4	1.8	1.8	Fine Sand
					2	1283.1	28.3	30.2	Coarse Sand
					3	2001.9	91.7	121.8	Gravelly sand
					4	901.6			Fine Sand
15	Ono, Ibiono	5.2556	7.8727	100	1	1119.1	3.4	3.4	Coarse Sand
					2	743.0	25.7	29.1	Fine Sand
					3	2211.0	73.8	103	Gravelly sand
					4	1157.4			Coarse Sand
16	Ikot Edok, Ibiono	5. 1821	7.9327	86	1	998.8	6.5	6.5	Fine Sand
					2	1450.8	121.2	127.7	Coarse Sand
					3	387.0			Clayey Sand
17	Nung Idio, Ikono	5.1668	7.8028	99	1	210.6	0.7	0.7	Clayey Sand
					2	1046.2	22.3	23.1	Coarse Sand
					3	1791.7	61.7	84.8	Gravelly sand
					4	454.1			Fine Sand
18	Aka Ekpeme, Ikono	5.174	7.7971	104	1	866.6	5.0	5.0	Fine Sand
					2	223.1	20.8	25.8	Clayey Sand
					3	189.9	48.5	74.3	Sandy Clay
					4	944.9			Fine Sand
19	Ikot Akpa Edok, Ikono	5.1708	7.7557	95	1	217.0	1.0	1.0	Clayey Sand
					2	94.5	75.2	76.2	Clay
					3	490.8			Fine Sand
20	Mbiakpan Ndiya, Ikono	5.1812	7.7552	103	1	530.2	1.4	1.4	Fine Sand
					2	145.4	5.7	7.1	Sandy clay
					3	2198.4	85.6	92.7	Gravelly sand
					4	906.0			Fine Sand
21	Nkwongho Ukpom, Ikono	5.1907	7.7548	113	1	642.3	1.1	1.1	Fine Sand
					2	342.2	11.7	12.9	Clayey Sand
					3	1350.4	71.7	84.6	Coarse Sand

					4	312.4			Clayey Sand
22	Ndiya Mfia, Ikono	5.2809	7.7413	127	1	295.6	1.1	1.1	Clayey Sand
					2	1148.9	104.1	105.2	Coarse Sand
					3	279.0			Clayey Sand
23	Obio Ediene, Ikono	5. 2095	7.8161	60	1	1051.1	1.9	1.9	Coarse Sand
					2	2471.1	21.9	23.8	Gravelly sand
					3	836.8	69.7	93.5	Fine Sand
					4	1505.8			Coarse Sand
24	Ndiya Ikot Imo, Ini	5.315	7.7015	135	1	70.8	2.1	2.1	Clay
					2	367.8	7.7	9.7	Clayey Sand
					3	1273.3	92.7	102.4	Coarse Sand
					4	416.1			Fine Sand
25	Mbiabong Ikpe, Ini	5.3299	7.6983	137	1	495.6	0.9	0.9	Fine Sand
					2	214.5	20.1	21	Clayey Sand
					3	1309.1	80.5	101.5	Coarse Sand
					4	874.2			Fine Sand
26	Ukwot Etok, Ini	5.3436	7.7093	130	1	199.7	4.5	4.5	Sandy clay
					2	996.7	43.2	47.7	Fine Sand
					3	333.9	72.6	120.3	Clayey Sand
					4	750.0			Fine Sand
27	Mbiakpa Ibakesi, Ini	5.3523	7.7258	119	1	1334.1	0.7	0.7	Coarse Sand
					2	411.8	9.7	10.4	Fine Sand
					3	2491.6	68.1	78.6	Gravelly sand
					4	580.3			Fine Sand
28	Odoro Ikpe, Ini	5.354	7.7502	117	1	1299.4	0.8	0.8	Coarse Sand
					2	462.5	6.3	7.1	Fine Sand
					3	2516.8	33.0	40.0	Gravelly sand
					4	1404.3	56.1	96.2	Coarse Sand
					5	478.6			Fine Sand
29	Nna Enin Ikpe, Ini	5.3682	7.7547	53	1	160.5	1.9	1.9	Sandy clay
					2	45.8	7.3	9.3	Clay
					3	562.2	16.1	25.4	Fine Sand
					4	2883.6	73.6	98.9	Gravelly sand
					5	791.9			Fine Sand
30	Ikpe Ikot Nkon, Ini	5.394	7.7786	33	1	353.6	2.2	2.2	Clayey Sand
					2	68.3	39.9	42.1	Clay
					3	180.2	51.6	93.8	Sandy clay
					4	931.5			Fine Sand

4.2.2 Ibiono Ibom Local Government Area

The geoelectric signatures across Ibiono Ibom (VES 7, 10 to 16) demonstrate structural continuity with deep, prolific hydrogeological zones.

Resistivity Profiles: Exceptional aquifer characteristics are observed at VES 10 (Okobo) and VES 11 (Ikot Efum), where deep gravelly sand horizons exhibit high resistivities of 3070.7 Ωm and 2801.5 Ωm, respectively.

Thickness and Spatial Depth: Thick sandy sequences are highly apparent at VES 16 (Ikot Edok), which presents a massive coarse sand layer extending down to 127.7 meters with a resistivity of 1450.8 Ωm. This points to thick, unconfined to semi - confined aquifer frameworks capable of sustaining high - yield groundwater extraction schemes.

4.2.3 Ikono Local Government Area

As the study transitions into Ikono LGA (VES 17 to 23), the geoelectric architecture shows a noticeable increase in fine-grained, argillaceous (clay-rich) sequences.

Clay and Sandy Clay Intercalations: A profound example of this lithological transition is captured at VES 19 (Ikot Akpa Edok), where a thick, low-resistivity clay aquitard (94.5 Ωm) spans from 1.0 meter down to a depth of 76.2 meters. Similarly, VES 18 (Aka Ekpeme) exhibits a prominent sandy clay layer with a low resistivity of 189.9 Ωm and a thickness of 48.5 meters.

Vulnerability Framework: These heavy clay and sandy clay horizons act as regional protective seals, shielding underlying fine-to-coarse sand aquifers (such as the 944.9 Ωm unit at VES 18) from surficial contamination paths.

4.2.4 Ini Local Government Area

Ini LGA (VES 24 to 30) represents the northernmost sector of the study area, exhibiting highly variable geoelectric characteristics influenced by the proximity to older, more consolidated structural formations.

Shallow Conducting Units: The topsoil and shallow horizons frequently consist of low-resistivity clays and sandy clays. This is prominent at VES 24 (Ndiya Ikot Imo: 70.8 Ωm surface clay), VES 29 (Nna Enin Ikpe: 45.8 Ωm clay), and VES 30 (Ikpe Ikot Nkon: 68.3 Ωm clay).

Deep Lithology: Despite the dense clay caps, deep-seated gravelly and coarse sand units maintain high transmissivity signatures, highlighted by the 2883.6 Ωm gravelly sand matrix at VES 29 occurring at a depth of 25.4 to 98.9 meters.

Generally, the integration of layer resistivity and thickness data provides the core baseline metrics for computing second-order geo-electrical indices; such as Longitudinal Unit Conductance (S), and Transverse Unit Resistance (T). In areas like Itu and Ibiono Ibom, where high-resistivity sands outcrop directly or lie beneath thin, permeable topsoil, the aquifer vulnerability index is inherently high due to negligible surficial resistance. Conversely, regions within Ikono and Ini LGAs that feature thick, low-resistivity clay sequences (such as VES 19 and VES 24) exhibit high longitudinal conductance values ($S = h/\rho$). These clay curtains serve as robust natural filters, attenuating migrating contaminant plumes and yielding low vulnerability indices. These 1D structural interpretations are validated continuously in the spatial domain by the 16 high-resolution 2D ERT profiles sampled in Figure 3, which effectively bridge the lateral lithological gaps between discrete sounding stations.

4.3. Interpretation of 2D ERT Profiles

Figure 3 presents one of the 16 2D ERT profiles acquired during the survey. This tomogram maps the spatial distribution of subsurface resistivity along the selected transect. Analyzing this profile alongside the others acquired for the study area allows for the mapping of structural weak points (such as fractures or missing clay layers) across the study area, providing the spatial raw data required for the eventual vulnerability zonation. The 2D tomograms were consolidated on the 1D VES curves to validate geoelectric parameters (such as, aquifer thickness, depth to water table, and protective capacity from the specific resistivity range of the protective aquitard to effectively drive the hybrid AHP–Entropy weighting and K-Means clustering model.

4.4 Interpretation of DRASTIC Index Parameters

4.4.1 Depth to Aquifer Index (D):

The spatial distribution of the Depth Index (D) in the DRASTIC aquifer vulnerability framework plays a critical role in controlling contaminant attenuation capacity, as deeper water tables provide a longer pathway through the unsaturated zone for physical, chemical, and biological degradation. The depth to aquifer index map is shown in Figure 5. The values of the depth index across the study area, range from a low of 5 (red/orange anomalies) to a high of 45 (bright green) regions.

In standard DRASTIC indexing, shallower water tables are assigned higher ratings/indices (yielding higher overall aquifer vulnerability), whereas deeper water tables correspond to lower depth indices (yielding lower vulnerability). High-Vulnerability Hotspots (Index; 5 to 15 / Red-Orange Anomalies): Concentrated clusters in western Ini, central Ikono, and south-central Ibiono Ibom reflect shallow groundwater tables (low depth index values). These localized depressions in depth to water indicate zones where surface contaminants can reach the saturated aquifer matrix with minimal attenuation time, denoting high inherent vulnerability. Low-Vulnerability Protective Zones (Index; 45 / Bright Green Regions): Dominating major parts of Itu, southern Ikono, and isolated sections of Ini, these high index values indicate deep groundwater tables. The extended unsaturated zone provides substantial filtration and sorption potential, conferring low to moderate aquifer vulnerability.

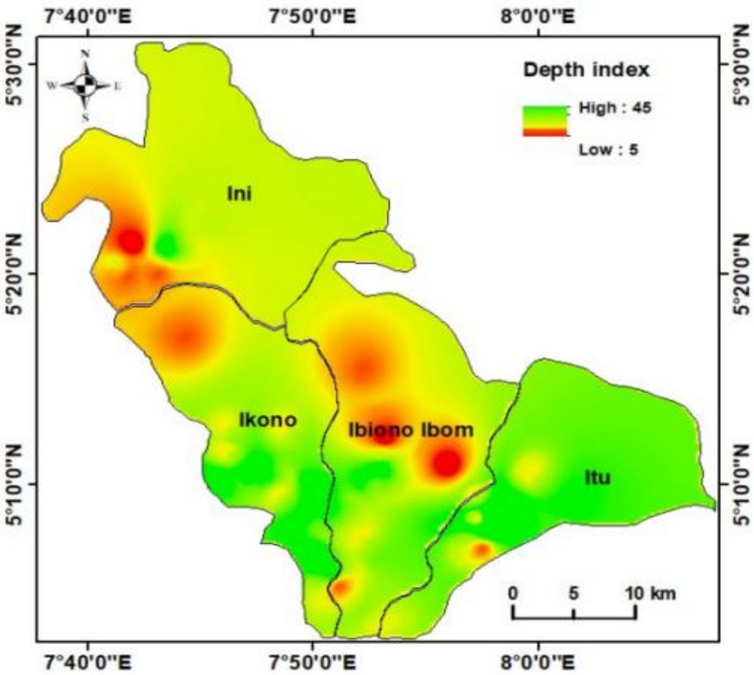

Figure 5: Depth to Aquifer Index Map

4.4.2 Net Recharge Index

Figure 6 illustrates the spatial distribution of the Net Recharge Index across the study area, with index values ranging from 12 (Red) to 40 (Green). The high index zones (Green), prominently concentrated in a distinct epicenter within central-western Itu, with moderate-to-high values (yellow-green) extending continuously across northern Ini. Low Index Zones (Red), heavily clustered in Ibiono Ibom, featuring a dominant low-recharge epicenter in its north-central sector, along with multiple red nodes along the boundary between southern Ikono and Ibiono Ibom. Intermediate Zones (Yellow), is the broad transition zones covering central Ikono and eastern Ibiono Ibom, bridging high and low recharge regions.

In groundwater vulnerability models (such as DRASTIC), the "Net Recharge" parameter quantifies the annual amount of water per unit area that percolates through the vadose zone to reach the water table. High Index (Green), indicates substantial water infiltration into the aquifer. High recharge volume acts as a primary vector for carrying surface-applied pollutants (such as; fertilizers, pesticides, waste leachates) down to the water table, leading to increased groundwater contamination risk. Low Index (Red), reflects restricted infiltration, typically caused by impermeable surficial layers or steep slopes that favor surface runoff. Lower recharge volume means less fluid is available to transport surface pollutants downward, providing higher relative protection to underlying groundwater.

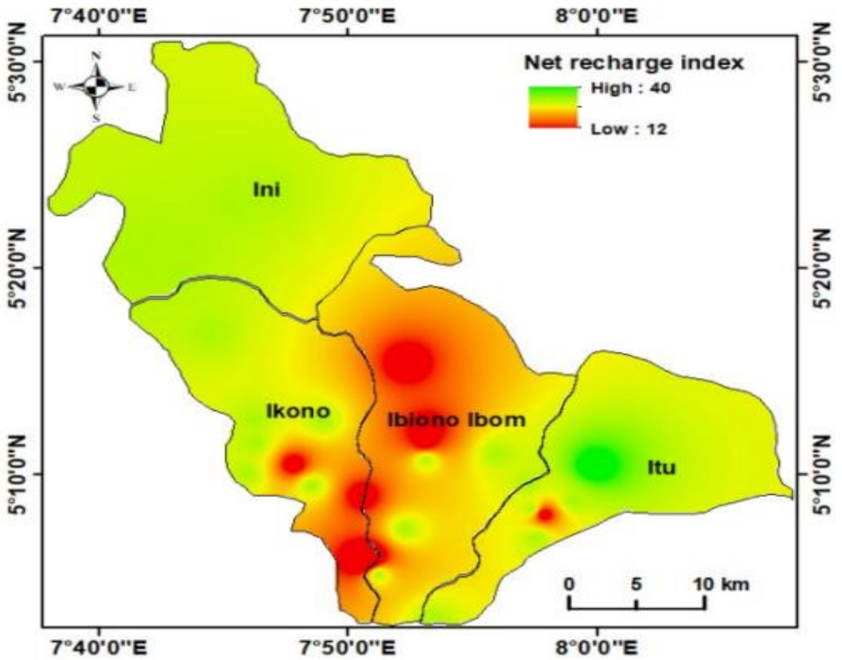

Figure 6: Net Recharge Index Map

4.4.3 Aquifer Media Index

Figure 7 displays the Aquifer Media Index across the study area. The index is represented via a color gradient where Green indicates a high index value (up to 24) and Red indicate a low index value (down to 9), with yellow and orange representing intermediate values. The highest aquifer media index values represented with green colour, are predominantly concentrated in the eastern portion of the map, specifically covering most of the Itu LGA. Other significant high-index pockets are visible in the northern part of Ibiono Ibom and the eastern edge of Ikono. The lowest values bearing the Red/Dark Orange are heavily concentrated in the western-central region of Ikono. Smaller, isolated nodes of low index values are also scattered across the central and southern portions of Ibiono Ibom. The transition intermediate Zones (Yellow/Light Orange), dominate the northernmost LGA, Ini, indicating a moderate aquifer media index throughout that specific region.

The "Aquifer Media" evaluates the material properties of the aquifer, which dictate groundwater flow and contaminant attenuation: the high index (Green; 24), typically represents coarser, highly permeable materials (like sand or gravel). These areas likely have higher groundwater yields but are more vulnerable to contamination because water (and potential pollutants) can move through the aquifer quickly with little filtration. The low index (Red; 9), typically represents finer, less permeable materials (like clay, silt, or fractured shale). These areas offer better natural protection against surface contamination due to slower flow rates and higher attenuation capacity, though they may yield less groundwater for extraction.

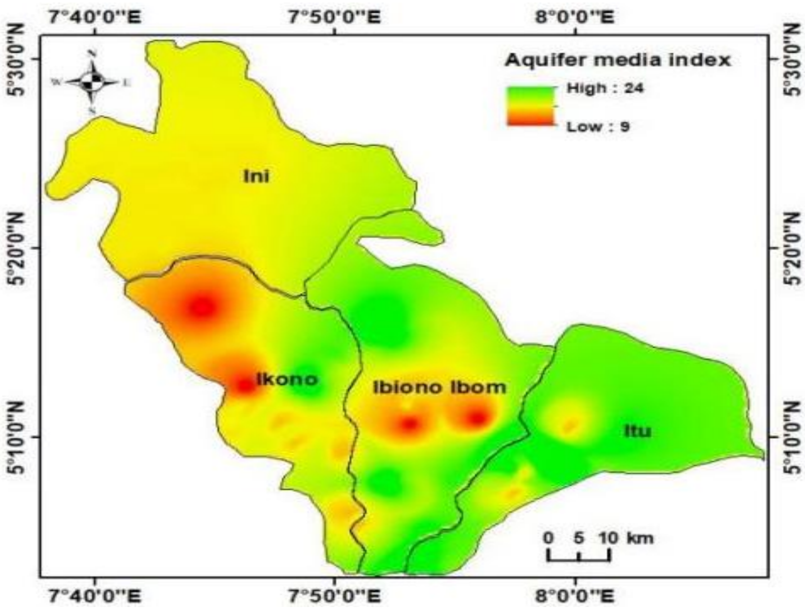

Figure 7: Aquifer Media index map

4.4.4 Soil Media Index

Figure 8 visualizes the Soil Media Index across the study area. The index is represented by a colour gradient where Green indicates a high index value (up to 20) and Red indicate a low index value (down to 2), with yellow and orange representing intermediate values. The highest soil media index values represented with green colour, are primarily concentrated in the central region of the map. There is a prominent green zone spanning the eastern part of Ikono and the northern half of Ibiono Ibom. A smaller, isolated green node is also visible on the western border of Ini. The lowest index values (Red/Dark Orange), are characterized by distinct, concentrated nodes. The most prominent low-index (red) zone dominates the southwestern portion of Itu. Other notable red zones exist in the northwestern part of Ikono and central Ini.

The Yellow/Light Orange, characterized by transitional intermediate zones, cover the majority of Ini and the outer edges of Itu, indicating moderate soil media index values across vast tracts of these LGAs. The "Soil Media" parameter evaluates the uppermost portion of the vadose zone, which influences how much precipitation infiltrates the ground versus how much runs off. The High Index (Green), typically indicates coarse-textured soils (like sand or sandy loam). These soils have high permeability, allowing surface water (and potential contaminants) to infiltrate rapidly downward into the groundwater system. Areas with high indices are more vulnerable to groundwater pollution. The low index (Red), typically indicates fine-textured soils (like clay or silty clay). These soils restrict the downward movement of water due to low permeability, promoting surface runoff instead. While they offer better natural protection for underlying aquifers against surface contaminants, these areas may be more prone to surface flooding or agricultural runoff issues.

4.4.5 Topography Index

Figure 9 is a visual display of the Topography Index across the study area. The index is mapped using a color gradient where Green denotes a high index value (up to 10) and Red denote a low index value (down to 6), with yellow and orange indicating intermediate transition zones. The study area is heavily dominated by high topography index values (Green). The entire northern expanse of Ini and the eastern expanse of Itu are almost uniformly green. Significant high-index tracts also cover the eastern and southern portions of Ibiono Ibom. The most striking feature of the map is a massive, highly concentrated low-index (deep red) anomaly dominating the northwestern sector of Ibiono Ibom. Several smaller, sharply defined low-index nodes are scattered across southern Ikono and near the western border of Itu. Intermediate Zones (Yellow/Light Orange), serve as tight transition buffers, primarily located in central Ikono, bridging the dominant green zones with the localized red anomalies.

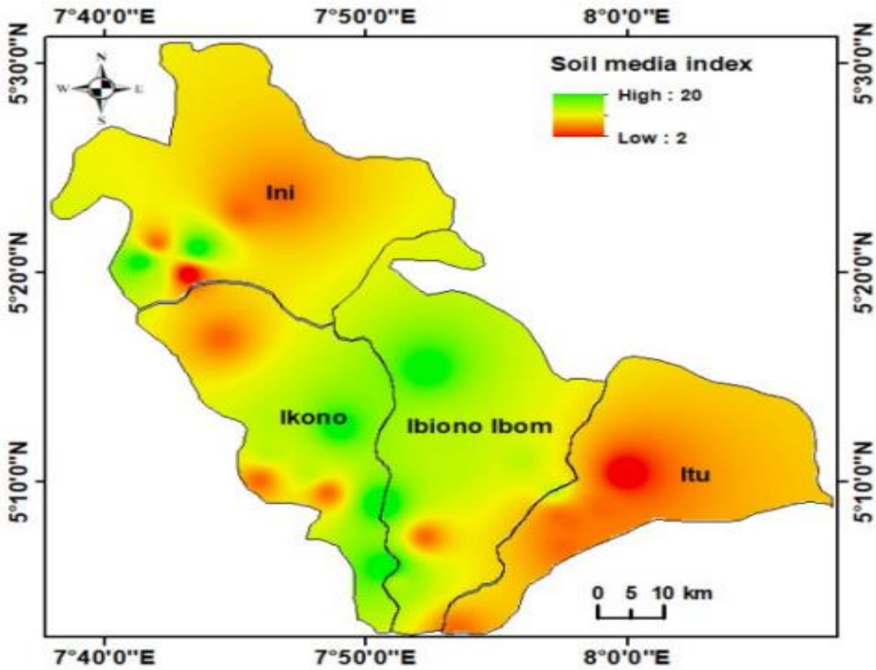

Figure 8: Soil Media index map

In standard environmental frameworks and groundwater vulnerability models (such as the DRASTIC model), this "Topography" parameter evaluates the slope or gradient of the land surface, which directly dictates water movement. High topography index (Green), represents flat terrain with very gentle slopes (typically 0-2%). Flat surfaces allow water to pool, minimizing runoff and maximizing the time available for downward infiltration. Consequently, these areas are highly vulnerable to groundwater contamination, as surface pollutants easily seep into the underlying aquifer. Low topography index (Red), represents steeper, more undulating terrain. Steeper slopes promote rapid surface water runoff and restrict the infiltration of water and pollutants. While these areas provide greater natural protection for underlying groundwater, the high runoff rates make them highly susceptible to topsoil erosion and surface-level contaminant transport to lower elevations.

4.4.6 Impact of Vadose Zone Index

Figure 10 illustrates the spatial variation of the impact of Vadose Zone Index across the study area. The parameter ranges from a low index value of 5 (Red) to a high value of 50 (Green), with yellow and orange marking intermediate values. The southern and eastern sectors are dominated with the high-index spectrum

(Green). Broad, continuous green expanses cover almost the entirety of Itu, Ibiono Ibom, and central-to-northern Ikono. Low-index values (Red), occur as tightly focused, isolated hotspots rather than regional trends. The most prominent clusters appear in central Ini, along the southwestern border of Ini, across the southern margin of Ikono, and at the southern tip of Ibiono Ibom. Intermediate Zones (Yellow), cover the majority of Ini, creating a broad buffer between its scattered low-index nodes and the high-index zones further south.

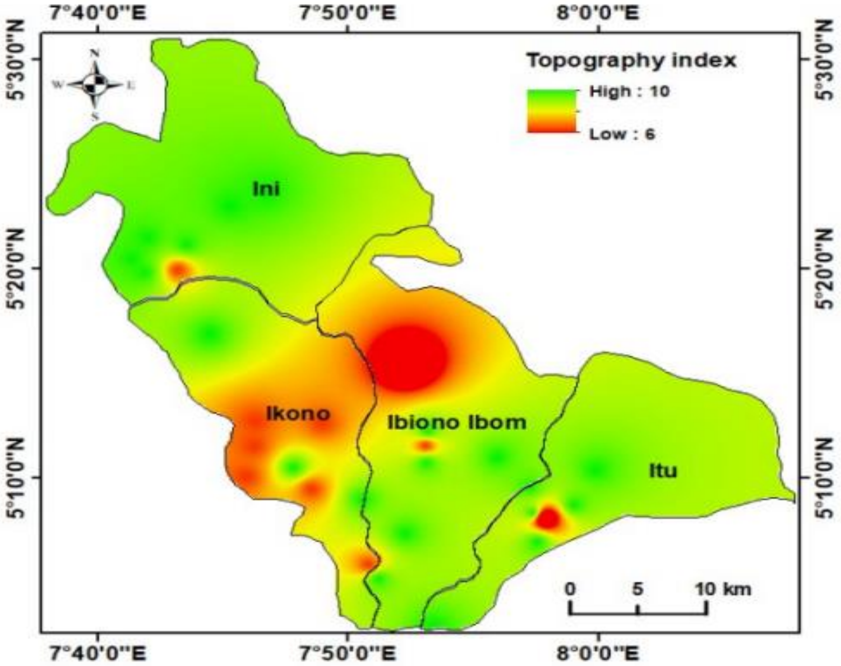

Figure 9: Topography Index map

The vadose zone represents the unsaturated layer between the land surface and the water table, serving as the primary geological barrier to vertical contaminant transport: High Index values (Green), corresponds to highly permeable media (such as sand or coarse gravel). Water and surface-derived pollutants percolate rapidly through these materials with minimal filtration, resulting in high groundwater vulnerability. Low Index (Red), on the other hand corresponds to dense, low-permeability media (such as clay or tight shale). These strata significantly retard downward fluid movement, providing strong natural attenuation and protection to the underlying aquifers.

4.5 Interpretation of Traditional Drastic Vulnerability Index Map

The resulting vulnerability map of the study area obtained from the traditional DRASTIC framework is shown in Figure 11, categorizing vulnerability into two distinct levels: moderate and low. The moderate vulnerability zone (Light Green) is the dominant rating across the entire study area. The vast majority of the area is shaded green, indicating a baseline of Moderate vulnerability to contamination. The Blue color represents pockets of low vulnerability scattered throughout the regions.

4.6 Quantitative Spatial Analysis of Hybrid DRASTIC Vulnerability Zonation

The integration of Machine Learning (ML) and Multi-Criteria Decision Analysis (MCDA) yielded a spatially explicit vulnerability profile for the study area. The hybrid model successfully delineated the regions into distinct vulnerability zones, optimized by ML predictive weights and MCDA spatial profiling. Unsupervised K-means clustering (K = 3) of the hybrid AHP-Entropy continuous DRASTIC vulnerability index partitioned the 1,240 km^2 study area into three distinct risk categories: (low, moderate and high) as shown in Figure 12. High Vulnerability Zone

(293.9 km^2 / 23.7%) showing orange colour on the map, concentrates primarily along central-eastern Ikono (35.4% of LGA area) and western-to-central Ibiono Ibom (35.4% of LGA area).

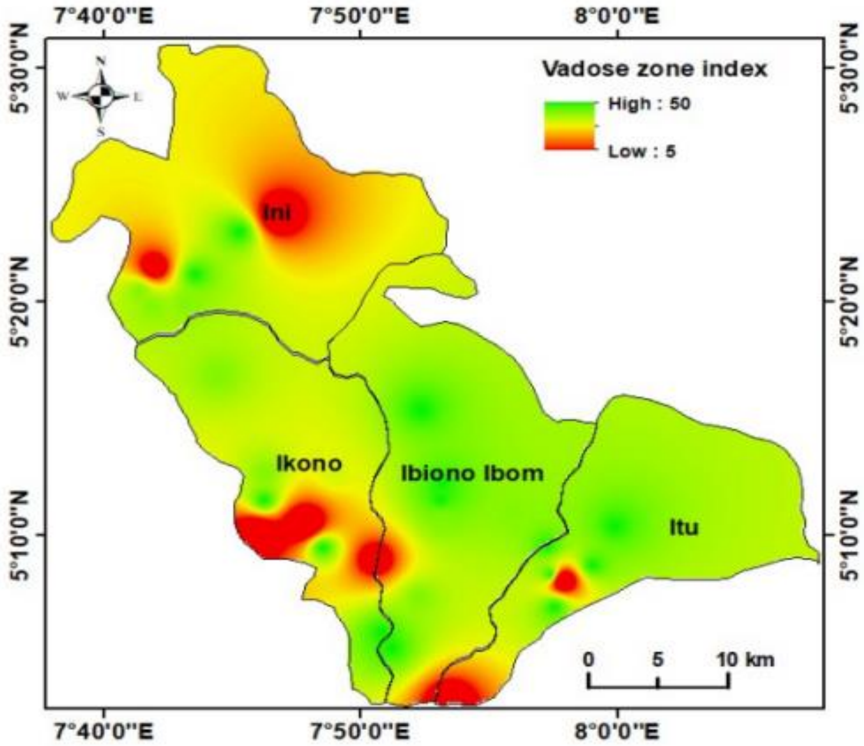

Figure 10: Impact of Vadose zone Index map

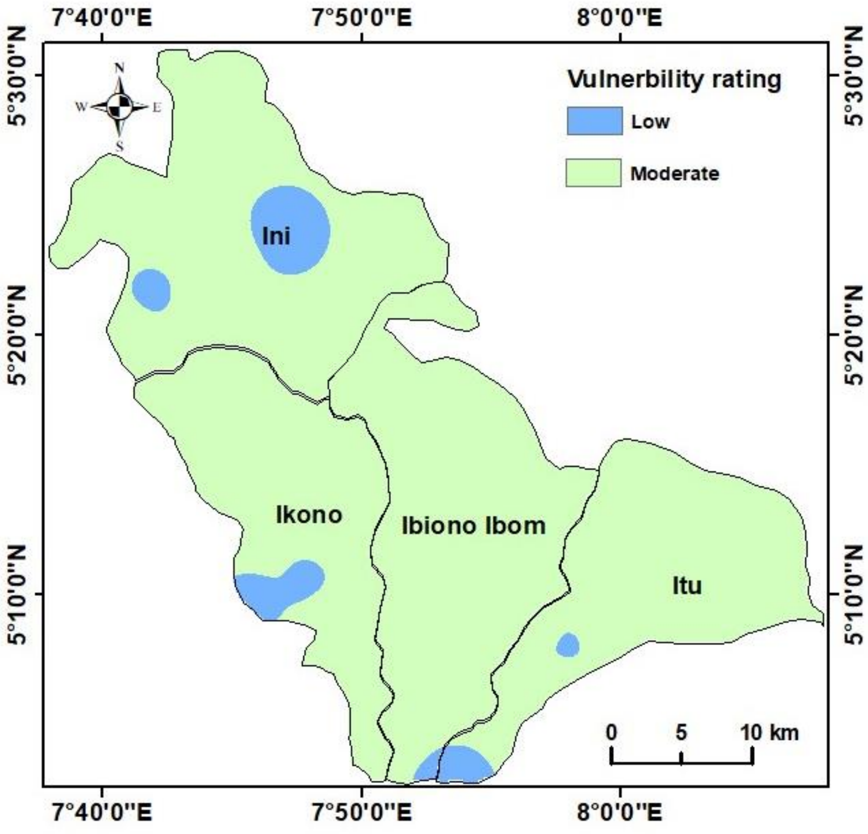

Figure 11: Traditional DRASTIC vulnerability rating map of study area

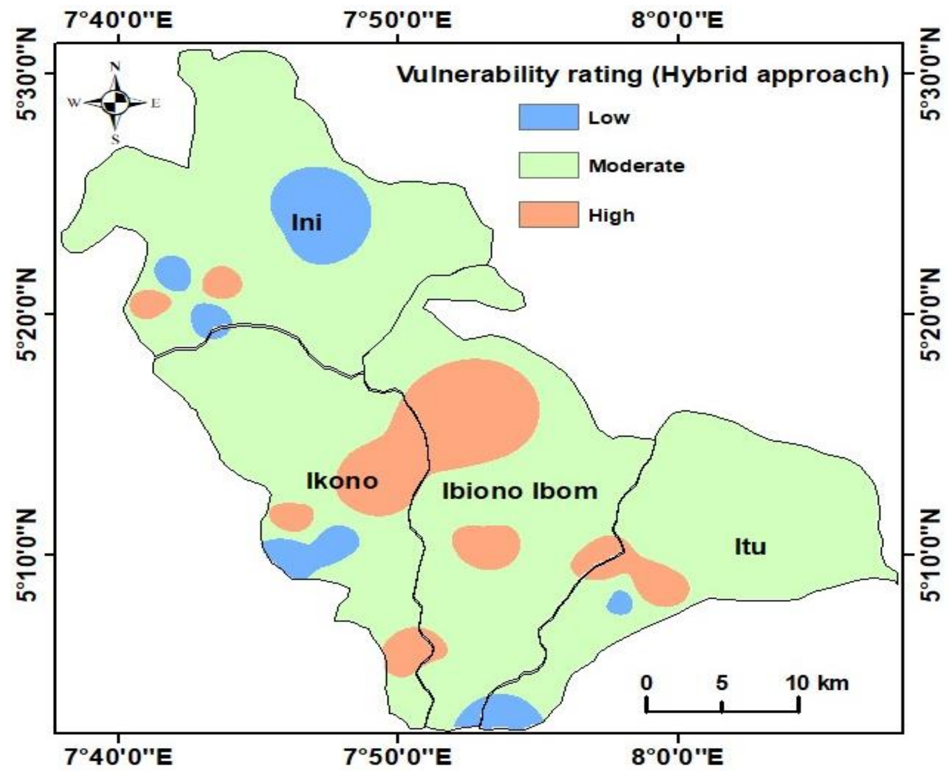

Figure 12: Hybrid DRASTIC Index Vulnerability map

These hotspots are governed by shallow groundwater depths (<15 m) and highly transmissive Benin Formation sand matrices, where effective vadose zone weights expand up to 51.03% due to minimal attenuation capacity. Moderate Vulnerability Zone (716.7 km^2 / 57.8%) having light green colour, forms the dominant background matrix across Itu (72.7%), Ini (59.3%), Ibiono Ibom (52.4%), and Ikono (50.8%). This widespread homogeneity reflects the regional baseline stability of intermediate topsoil permeability and gentle terrain slopes (0-5%). Low Vulnerability Zone (229.4 km^2 / 18.5%) showing sky blue colour are predominantly located in northern Ini (35.2% of LGA area) and northern Ibiono Ibom (12.2%). Hydrogeologically, these protective shields are sustained by dense, low-permeability clay aquitards within the Imo Shale and Ameki Formations, where high longitudinal conductance values ($S = h/\rho$) effectively block downward contaminant transport.

4.6.1 Overall Study Area Vulnerability Proportions

The total study area covers approximately 1, 240 km^2 across the four Local Government Areas (LGAs). Unsupervised K-means spatial clustering of the 30 m × 30 m raster cells yields the following overall regional distribution:

Low Vulnerability Class: 229.4 km^2 (18.5 %), Moderate Vulnerability Class: 716.7 km^2 (57.8%), High Vulnerability Class: 293.9 km^2 (23.7%). Table 12 is the structured table derived from the spatial pixel breakdown across Itu, Ibiono Ibom, Ikono, and Ini LGAs.

4.6.2 VES Point Distribution Across Vulnerability Classes

Evaluating the discrete 30 Vertical Electrical Sounding (VES) station coordinates against the optimized K-means vulnerability classes demonstrates how field sampling points reflect regional spatial zonation:

High Vulnerability VES Points (9 stations / 30.0%), comprising; VES 4, VES 6, VES 7, VES 10, VES 13, VES 14, VES 17, VES 21, VES 23. This vulnerability class is characterized by shallow water tables, highly transmissive coarse/gravelly sand matrices, and thin or permeable topsoil covers.

Moderate Vulnerability VES Points (15 stations / 50.0%), comprising; VES 2, VES 5, VES 8,

VES 9, VES 11, VES 12, VES 15, VES 16, VES 20, VES 22, VES 25, VES 26, VES 27, VES 28. this class represent the dominant background matrix with intermediate depth-to-water and alternating sand-silt-clay sequences.

Low Vulnerability VES Points (6 stations / 20.0%), spanning across VES 1, VES 3, VES 18, VES 19, VES 24, VES 29, VES 30, are shielded by thick, low-resistivity clay/shale aquitards (e.g. VES 19 with a 75.2 m thick clay unit).

Table 12: Vulnerability Distribution by Local government Area

LGA	LGA Area Share (%)	Low Vulnerability (%)	Moderate Vulnerability (%)	High Vulnerability (%)
Itu	22.2	18.2	72.7	9.1
Ibiono Ibom	29.8	12.2	52.4	35.4
Ikono	26.2	13.8	50.8	35.4
Ini	21.8	35.2	59.3	5.5
Total / Regional Mean	100.0	18.5	57.8	23.7

4.6.3 Relationship Between Vulnerability and Subsurface Lithology

High Vulnerability Hotspots (23.7% of area), correlates directly with the unconsolidated, continental quartz sands of the Benin Formation in southern Ikono and western Ibiono Ibom. The absence of continuous clay beds combined with coarse, gravelly sand matrices (resistivities exceeding 2,000 Ωm) provides high porosity and hydraulic conductivity, facilitating rapid vertical and lateral contaminant movement. Moderate Vulnerability Matrix (57.8% of area), corresponds to the transitional Ogwashi-Asaba Formation and Alluvium deposits, characterized by interbedded sequences of fine-to-coarse sands, silts, and thin clay lenses that provide moderate filtration capacity. Low Vulnerability Shields (18.5% of area), strongly aligned with the marine shales and argillaceous units of the Imo Shale and Ameki Formations in northern Ini and northern Ibiono Ibom. Thick, low-resistivity clay sequences (45.8–94.5 Ωm) act as geomechanical barriers that retard fluid migration.

4.6.4 Relationship Between Vulnerability and Groundwater Depth

A. Inverse Spatial Correlation: A strong inverse relationship exists between static water level (SWL) depth and vulnerability risk. High vulnerability hotspots coincide with areas where depth-to-water is extremely shallow (< 15 m).

B. Sensitivity Analysis Validation: Map Removal Sensitivity Analysis identified Depth to Water as the most critical global parameter with a mean sensitivity shift of 5.21% (and a maximum spike of 7.61%). Shallow water tables reduce vertical attenuation time to near zero, causing localized vulnerability scores to increase sharply.

4.6.5 Relationship Between Vulnerability and Vadose-Zone Thickness and Composition

A. Primary Localized Driver: Single-Parameter Sensitivity Analysis revealed that the Impact of the Vadose Zone is the single most dominant localized driver in the study area, with its mean effective weight expanding from a theoretical 27.52% to an effective 36.67%.

B. Attaching Mechanics: In zones where the vadose layer is dominated by thick clay or sandy clay seals (example, VES 19 and VES 24), vertical percolation rates decrease substantially, resulting in Low Vulnerability zonation. Where the vadose zone consists of porous, coarse sand, effective weights spike up to 51.03%, driving acute High Vulnerability classifications.

4.7 Cluster Optimization and Validation Results

4.7.1 The Elbow Plot

To establish the optimal number of clusters (k) for partitioning the continuous hybrid vulnerability index without introducing manual bias, the Elbow Method was implemented. The generated Elbow Plot is shown in Figure 13.

As shown in the plot (Figure 13), the WCSS decreased progressively with increasing k, with a marked reduction up to k = 3 and a smaller incremental improvement thereafter, creating a distinct "elbow" or inflection point. This pattern, together with the Silhouette analysis, supports k = 3 as a reasonable clustering solution.

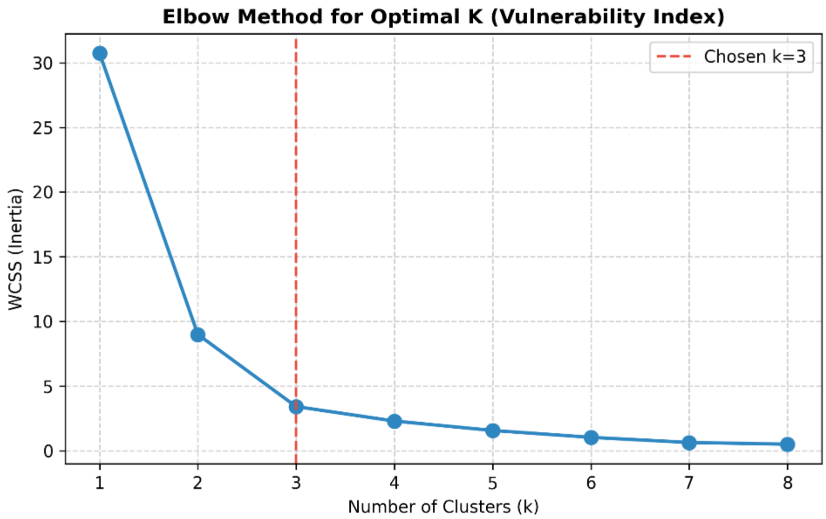

Figure 13: Elbow plot for optimal k

4.7.2 Clustering Performance and Internal Validation Metrics

The empirical results of clustering performance and internal validation metrics are compiled in Table 13. Minimum WCSS means the algorithm has successfully converged to a state where inner-cluster variance cannot be reduced any further without adding more clusters (Table 13). The calculated Silhouette Coefficient of 0.62 demonstrates that the individual VES points are highly aligned with their designated risk vectors and well-separated from neighboring threshold, indicating a highly successful grouping as defined by Rousseeuw (1987). This is further validated by a low Davies-Bouldin Index of 0.44, which establishes that the mathematical distance between the centroids of different vulnerability zones significantly exceeds the dispersion within each individual zone (Davies and Bouldin, 1979). Lastly, the high Calinski-Harabasz Index (108.03) mathematically proves that the transition from low-susceptibility zones to acute-vulnerability zones represents distinct hydrogeological regimes rather than arbitrary statistical increments (Caliński and Harabasz, 1974). However, the present validation evaluates the internal statistical structure of the vulnerability classes rather than independent contaminant occurrence.

4.8 Sensitivity Analysis results

4.8.1 Map removal

The results of the map removal sensitivity analysis are summarized in Table 14, comprising the mean variation, minimum and maximum bounds, and the coordinate standard deviation across the 30 VES stations. Table 13 shows that the depth parameter constitutes the primary determinant of aquifer contamination risk within the study area, exhibiting a dominant mean index sensitivity of 5.21%. From a hydrogeological perspective, this high sensitivity indicates that localized fluctuations in the unsaturated zone's thickness exert a primary control over the travel time and physical attenuation of downward - percolating anthropogenic contaminants.

Table 13: K-means Clustering Evaluation and Partition Metrics Results

Validation metrics	Computed values	Theoretical ideal	Architectural interpretation
Silhouette Coefficient	0.62	1	Indicates robust cluster assignment with no significant overlapping boundaries
Calinski-Harabasz Index	108.03	∞	Confirms high between-cluster variance and tight within-cluster homogeneity
Davies-Bouldin Index	0.44	0	Demonstrates excellent separation; cluster centroids are far apart relative to their internal spread
Final Residual Inertia (WCSS)	3.41	Minimum	Represents the minimized cumulative error at the k = 3 convergence limit.

Table 14: Map Removal Sensitivity Analysis Result

Parameter Removed	Mean Sensitivity (%)	Minimum Sensitivity (%)	Maximum Sensitivity (%)	Standard Deviation (%)
Depth	5.21	0.49	7.61	1.66
Soil media	2.85	0.67	5.56	1.4
Aquifer media	2.8	1.45	3.52	0.49
Hydraulic conductivity	2.38	2.38	2.38	0
Impact of vadose zone	2.36	0.06	7.32	2.05
Topography	1.96	1.18	2.42	0.27
Net recharge	1.7	0.1	3.61	0.79

The wide range between its minimum (0.49%) and maximum (7.61%) limits underscores the spatial variance of the unconfined water table across the mapped sub-basins. Following the depth parameter, the Soil Media and Aquifer Media display moderate-to-high mean sensitivities of 2.85% and 2.80%, respectively. These parameters function as critical structural filters; variations in surficial soil texture and the underlying saturated porous media directly dictate the physical mechanisms of hydraulic sorting, adsorption, and vertical contaminant migration paths. Conversely, Topography and Net Recharge exhibit the lowest comparative mean sensitivities at 1.96% and 1.70%, respectively. This statistical profile indicates that within this specific spatial data network, topography and net recharge parameters play secondary roles in actively differentiating distinct groundwater vulnerability zones.

A notable statistical profile is observed in the behavior of Hydraulic Conductivity, which generated a mean, minimum, and maximum sensitivity of exactly 2.38%, resulting in a standard deviation of 0.00%. In conventional index-overlay operations, a standard deviation of zero indicates that a parameter layer acts as a uniform spatial scalar rather than a geographic differentiator. Because the empirical input values for hydraulic conductivity derived from the geophysical soundings are completely homogeneous across all 30 VES stations, the layer injects an identical baseline value into both the unperturbed (V) and perturbed (V') index calculations. While the layer retains a minor mathematical footprint within the unified index due to its foundational AHP weight configuration, its zero variance highlights a critical diagnostic reality: the layer provides no unique information to help geographically delineate risk boundaries. This empirical outcome serves as strong validation for the methodology integrated into this study. By pairing subjective AHP assumptions with Shannon's Information Entropy, the framework successfully penalized and managed non-informative, stagnant layers that would otherwise artificially inflate or skew spatial vulnerability classifications.

The coordinate standard deviation (SD) column yields critical insights into the internal structural variance and anisotropy of the underlying hydrogeological formations. While parameters such as aquifer media (SD = 0.49%) and topography (SD = 0.27%) demonstrate highly consistent, spatially stable impacts across the study domain, the Impact of the Vadose Zone displays the highest structural dispersion with a standard deviation of 2.05%, spanning a wide continuum from a minimum of 0.06% to a maximum of 7.32%. This notable statistical spread mathematically confirms the presence of acute localized heterogeneity within the unsaturated vadose layers. In zones where the sub-surface lithology shifts rapidly between highly permeable, porous sands (evidenced by the high maximum variation boundary of 7.32%) and tight, protective clay or shale aquitards (represented by the minimum boundary of 0.06%), the model's output relies heavily on the presence of the vadose zone impact parameter. This extreme variance proves that the vadose zone acts as an irregular, geologically complex structural shield across the study area, confirming that a rigid, non-optimized DRASTIC configuration would fail to accurately capture the true local hydrogeological dynamics.

4.8.2 Single parameter sensitivity analysis

The results of the single parameter sensitivity analysis are compiled in Table 15. A comparative analysis between the constant Theoretical Hybrid Weight (%) and the calculated Mean Effective Weight (%) which reveals significant spatial and functional shifts across the study area.

Table 14: Results of single parameter sensitivity analysis

Parameter	Theoretical Hybrid Weight (%)	Mean Effective Weight (%)	Min. Effective Weight (%)	Max. Effective Weight (%)	Standard Deviation (%)
Ir	27.52	36.67	6.04	51.03	13.64
Sr	18.76	16.72	3.29	34.4	7.37
Dr	27.7	16.56	5.02	54.72	10.14
Rr	11.31	15.15	4.79	26.83	4.61
Ar	11.17	8.92	5.09	16.15	2.62
Tr	3.55	5.99	3.3	10.52	1.58
Cr	0	0	0	0	0

According to Table 14, the most reflective structural manifestation occurs within the Impact of the Vadose Zone layer. While vadose zone impact was assigned an already high theoretical hybrid weight of 27.52%, its mean effective weight expanded to 36.67%, establishing it as the most critical driver of aquifer vulnerability in this geological setting. From an environmental hydrogeology standpoint, this upward escalation indicates that the specific lithological structures and pore-space distributions within the unsaturated vadose layers are highly active. The extreme range between its minimum effective weight (6.04%) and its maximum effective weight (51.03%) reflects severe localized shifts in subsurface sealing properties - moving dynamically from protective, clay-rich layers that reduce risk to highly transmissive, unconfined porous sands that aggressively amplify contaminant transport.

On the other hand, the depth parameter exhibits a substantial structural compression. Despite holding the highest baseline structural weight at 27.70%, its mean effective weight dropped to 16.56%. This downward shift proves that while water table depth is conceptually critical, the localized depth variations across a majority of the sounding points are subdued relative to the overriding filtering capacity of the overlying vadose zones and surficial soils (mean effective weight of 16.72%). However, the massive upper bound of depth parameter reaching 54.72% indicates that at specific, acute localized coordinates, a dramatically shallow water table completely overwhelms all other protective layers, instantly shifting those specific points into high vulnerability zones.

Among the intermediate parameters, Net Recharge and Topography both demonstrated field-level amplification. Net recharge shifts upward from a theoretical weight of 11.31% to a mean effective weight of 15.15%. This reveals that atmospheric infiltration and deep percolation volumes are actively interacting with local infiltration pathways, magnifying the vulnerability risk beyond the a priori weight configurations. Topography nearly doubled its functional impact, moving from a marginal theoretical weight of 3.55% to a mean effective weight of 5.99%. This mathematically confirms that even minor topographic depressions and slope gradients across the study area act as focal collection points, artificially intensifying the localized hydraulic head of surface runoff and accelerating vertical infiltration. In contrast, Aquifer Media exhibits a modest reduction, dropping from a theoretical weight of 11.17% to a mean effective weight of 8.92%. This minor suppression demonstrates that within this specific spatial data network, the physical parameters governing the sub-surface saturated storage are structurally subordinate to the surficial and vadose throttling layers that dictate whether a contaminant can even breach the water table.

The standard deviation column provides an empirical index of the study area's internal geological heterogeneity and structural anisotropy. Parameters such as Topography (standard deviation = 1.58%) and Aquifer Media (standard deviation = 2.62%) display narrow statistical dispersion, demonstrating that their mechanical influence remains highly uniform and predictable across the geographic coordinates. The Impact of the Vadose Zone exhibited the highest mean effective weight in the single-parameter analysis, indicating strong localized influence on the vulnerability index. Depth to Water (with Maximum effective weight of 54.72%), exhibited the highest mean sensitivity in the map-removal analysis, indicating that it was the most influential parameter in the overall index under the adopted weighting scheme. In an isotropic, homogenous structural basin, effective weights cluster tightly around their means. Here, the expansive standard deviations prove that the aquifer system is highly segmented and anisotropic. The vast spacing between the minimum and maximum effective boundaries demonstrates that a single, rigid, non-optimized weighting framework is fundamentally incapable of capturing localized risk realities. The zero spatial variation obtained for hydraulic conductivity indicates that this parameter contributed little to spatial differentiation in the present dataset. However, the uniformity should be independently examined to determine whether it reflects genuine hydrogeological conditions or limitations in the estimation and interpolation of hydraulic conductivity.

4.9 Comparative Analysis of Traditional versus Hybrid DRASTIC Vulnerability Mapping

A visual and structural comparison between the traditional DRASTIC framework (Figure 11) and the optimized Hybrid AHP-Entropy K-Means model (Figure 12) shows significant limitations in standard index-overlay routines. The traditional model categorizes the study region into only two broadly defined classifications: Low Vulnerability (isolated blue pockets) and an overarching, monolithic Moderate Vulnerability matrix (light green) that spans across Ini, Ikono, Ibiono Ibom, and Itu Local Government Areas. By failing to integrate information entropy and advanced data clustering, the traditional map suffers from severe spatial smoothing - fundamentally obscuring acute, high-risk contamination pathways.

The most striking defect of the traditional map (Figure 11) is the complete absence of any High Vulnerability zones. In traditional mapping, human-defined, rigid scoring intervals (example, classifying risk based on flat arbitrary brackets like 100–120 or 120–140) create an artificial mathematical averaging effect. When highly sensitive local parameters are coupled with flat, non-informative variables, the high-risk values are mathematically washed out. The model forces the entire southern half of the study area - spanning central Ikono and western Ibiono Ibom into a uniform Moderate classification. When compared against the Single-Parameter Sensitivity Analysis (SPSA) metrics, this traditional smoothing is hydrogeologically invalid. The SPSA proved that at specific coordinates, the effective weight of Depth to Water violently spikes to an upper bound of 54.72%. In the traditional map, this localized danger is entirely masked. By contrast, the Hybrid K-Means model reads these massive point-by-point fluctuations and dynamically carves out the continuous High Vulnerability Hotspots (the orange/coral zones in Figure 12) across central Ikono and western Ibiono Ibom. This demonstrates that your hybrid model successfully exposes real-world areas where an exceptionally shallow water table makes the aquifer immediately vulnerable to surficial pollutant loads.

The two frameworks also diverge sharply in how they delineate protective boundaries. In the traditional map (Figure 11), the Low Vulnerability zones exist as highly restricted, rigid geometries - primarily clustered in central Ini, with tiny, isolated anomalies in western Ini, southern Ikono, and southern Ibiono Ibom. This rigid distribution occurs because traditional DRASTIC applies fixed, subjective AHP weights globally across the entire map, treating the unsaturated zone as a spatially uniform layer. The hybrid framework (Figure 12) profoundly restructures these protections. In the optimized map, the low-vulnerability anomaly in northern Ini expands into a continuous, naturally shaped continuous zone. Simultaneously, new distinct, circular low-risk pockets emerge along the western margins of Ini and Ikono. This spatial modification is fully supported by the sensitivity analyses, which revealed that the **I**mpact of the Vadose Zone possesses the highest statistical volatility in the entire system (SD = 13.64%). Where the traditional model forces Impact of the Vadose Zone to conform to a static desktop baseline, the hybrid model allows the layer's effective weight to organically expand to its true field maximum of 51.03%. The resulting map accurately isolates regions shielded by dense, low-permeability clay-rich lenses or heavy silt beds, optimizing the delineation of natural structural protection.

The structural transition from the traditional map to the hybrid map highlights a major advancement in data science. Traditional mapping relies on an unverified assumption of spatial homogeneity. However, the dual sensitivity analysis mathematically proved that the study area is highly anisotropic, characterized by immense local weight swings in vertical transport layers (Impact of the Vadose Zone swinging from 6.04% to 51.03%; depth swinging from 5.02% to 54.72%). Because the parameters shift so dramatically from one VES station to another, applying arbitrary, human-defined breaks is mathematically invalid. This volatility rendered unsupervised K-means clustering a methodological necessity.

By utilizing the algorithm to minimize internal variance (WCSS) to its true mathematical limit, the final boundary lines were drawn dynamically by the data structure itself. Furthermore, by utilizing Shannon's Information Entropy, the hybrid model completely neutralized the uninformative Hydraulic Conductivity parameter (SD = 0.00%), stripping away background noise that would otherwise distort the map. The resulting hybrid framework successfully shifts groundwater vulnerability mapping from a static desktop index to an adaptive, and optimized sub-surface diagnostic tool.

4.10 Comparative Assessment with Previous Studies in the area

The findings of this hybrid MCDA-ML framework align well with and refine past hydrogeological investigations conducted across Akwa Ibom State and the broader southeastern Niger Delta Basin. Standard DRASTIC, GOD, and AVI assessments in adjacent coastal and hinterland sectors (for example, Ekanem, 2022; Udosen et al., 2023, 2024a) historically mapped extensive, unconstrained "High" vulnerability zones due to the thick, porous sand horizons of the Benin Formation. However, those empirical index applications often over-estimated risk along northern transition boundaries because they could not mathematically account for spatial variance or localized clay interleaving. By incorporating Shannon's Information Entropy and Unsupervised K-Means clustering, the present study resolves those broad generalizations. The identification of high vulnerability hotspots in the southern Benin Formation plain corridors agrees directly with the high effective porosity and low protective capacity mapped by George et al. (2022a, b) and Ekanem et al. (2024b). Furthermore, the delineation of low vulnerability shields in the northern sector (Ini and northern Ibiono Ibom) provides quantitative validation for the structural clay/shale aquitard protections described by Udo et al. (2023) and Ekpo et al. (2024) within the Ameki and Imo Shale Formations. Furthermore, by neutralizing non-informative layers like hydraulic conductivity (0.00% effective variance), this work addresses the key methodological limitations raised by Ekanem and Ebong (2026), proving that data-driven ML-MCDA hybridization yields significantly improved spatial boundary resolution relative to traditional empirical overlay models.

5.0 Conclusion

The integrated AHP-entropy-K-means DRASTIC framework provided a spatially differentiated assessment of groundwater vulnerability across the study area. The results identified three vulnerability classes, with high vulnerability concentrated mainly in areas characterized by shallow groundwater and permeable sandy materials, while relatively protected zones were associated with clay-rich vadose and aquifer materials. Depth to water exhibited the highest mean sensitivity in the map-removal analysis, whereas the Impact of the Vadose Zone had the highest mean effective weight in the single-parameter analysis. Hydraulic conductivity showed no spatial variation in the present dataset and therefore contributed little to spatial differentiation. These findings demonstrate the usefulness of combining geophysical characterization with objective weighting and unsupervised clustering, although independent groundwater-quality data are still required for external validation of the vulnerability classes.

Acknowledgements

The authors express their sincere gratitude to the Akwa Ibom State Rural Water Supply and Sanitation Agency (AK-RUWATSAN) for providing borehole lithology logs for calibration and validation. Special thanks to the technical field crews whose support was invaluable during the 1D VES and 2D ERT geophysical data acquisition campaigns across the study area. Contact persons, including youth and community leaders of Itu, Ibiono Ibom, Ikono, and Ini Local Government Areas who allowed access to their communities during the survey are equally appreciated.

References

Akankpo, A. O., Igboekwe, M. U., & Udoinyang, I. E. (2018). Hydro-geophysical investigation of groundwater potential in parts of Akwa Ibom State, Southeastern Nigeria. *Journal of Applied Sciences and Environmental Management*, 22(4), 511–517.

Al-Adamant, K., Othman, A., & Ibrahim, M. (2003). Groundwater vulnerability mapping of the Gaza Strip using GIS. *Journal of Environmental Management*, 69(4), 389 – 398.

Aller, L., Bennett, T., Lehr, J. H., Petty, R. J., & Hackett, G. (1987). DRASTIC: A standardized system for evaluating ground water pollution potential using hydrogeologic settings. *US Environmental Protection Agency, Office of Research and Development*, EPA/600/2-87/035, Washington, D.C.

Amiri, V., Rezaei, M., & Kujawski, W. (2020). A critical review on the use of GIS-based water quality indices (WQIs) in groundwater. *Ecological Indicators*, 115, Article 106368.

Asfahani, J., Aretouyap, Z., & George, N. (2023) Hydraulic characterization of the Adamawa-Cameroon aquifer using inverse slope method. *Water Practice and Technology* (2023) 18 (3): 547–562. https://doi.org/10.2166/wpt.2023.033

Babiker, I. S., Mohamed, M. A., Hiyama, T., & Nishigaki, M. (2005). A GIS-based DRASTIC model for assessing aquifer vulnerability in Kakamigahara Heights, Gifu Prefecture, central Japan. *Science of the Total Environment*, 345(1-3), 127–140.

Caliński, T., & Harabasz, J. (1974). A dendrite method for cluster analysis. Communications in Statistics-Theory and Methods, 3(1), 1–27.

Davies, D. L., & Bouldin, D. W. (1979). A cluster separation measure. IEEE Transactions on Pattern Analysis and Machine Intelligence, (2), 224–227.

Dobrin, M. B., & Savit, C. H. (1988). Introduction to Geophysical Prospecting (4th ed.). McGraw-Hill, New York.

Ebong, E. D., Akpan, A. E., & Onwuegbuche, A. A. (2017). Estimation of geoelectric and hydraulic parameters of aquifers in parts of Uyo Local Government Area, Akwa Ibom State, Southeastern Nigeria. *Journal of African Earth Sciences*, 129, 732–744.

Ekanem, A. M. (2022). AVI- and GOD-based vulnerability assessment of aquifer units: a case study of parts of Akwa Ibom State, Southern Niger Delta, Nigeria. *Sustainable Water Resources Management*, 8, 29. https://doi.org/10.1007/s40899-022-00628-x

Ekanem, A. M., & Ebong, S. T. (2026). Hybrid DRASTIC–Machine Learning Framework for Groundwater Vulnerability Assessment in parts of Akwa Ibom State, Nigeria. *Intelligent Geoengineering*, https://doi.org/10.1016/j.ige.2026.07.001

Ekanem, A. M., George, N. J., Thomas, J. E., & Udo, I. G. (2024). Geophysical investigation of aquifer flow unit characteristics in northern parts of Akwa Ibom State, Southern Nigeria. *Results in*

Earth Sciences, 2, 100017. https://doi.org/10.1016/j.rines.2024.100017

Ekanem, A. M., Akpan, A. E., George, N. J. & Thomas. J. E. (2021). Appraisal of protectivity and corrosivity of surficial hydrogeological units via geo-sounding measurements. *Environ Monit Assess* 193, 718. https://doi.org/10.1007/s10661-021-09518-9

Ekpo, A. E., Bassey, N. E., George, N. J., & Udo, I. G. (2024). Depth to basement estimation from aerogravity data over the Southeastern part of Niger Delta region of Nigeria. *Researchers Journal of Science and Technology*, 4(5), 44 – 66. https://doi.org/10.83080/rejost.vol4no5.135

Fetter, C. W. (1994). Applied hydrogeology (3rd ed.). Prentice Hall.

George N. J. (2021a). Geo-electrically and hydrogeologically derived vulnerability assessments of aquifer resources in the hinterland of parts of Akwa Ibom State, Nigeria. *Solid earth sciences*, 6(2), 70-79. https://doi.org/10.1016/j.sesci.2021.04.002.

George, N. J. (2021b). Modelling the trends of resistivity gradient in hydrogeological units: a case study of alluvial environment. *Model. Earth Syst. Environ.* **7**, 95–104. https://doi.org/10.1007/s40808-020-01021-3

George, N. J., Atat., J., Umoren, E. B., & Etebong, I. (2017) Geophysical exploration to estimate the surface conductivity of residual argillaceous bands in the groundwater repositories of coastal sediments of EOLGA, Nigeria *NRIAG Journal of Astronomy and Geophysics*, 6 (1), 174-183

George, N. J., Bassey, N. E., Ekanem, A. M., & Thomas, J. E. (2020). Effects of anisotropic changes on the conductivity of sedimentary aquifers, southeastern Niger Delta, Nigeria. *Acta Geophysica,* 68, 1833–1843. https://doi.org/10.1007/s11600-020-00502-4

George, N. J., Ekanem, K. R., Ekanem, A. M. Udosen, N. I. & Thomas J. E. (2022a). Generic comparison of ISM and LSIT interpretation of geo-resistivity technology data, using constraints of ground truths: a tool for efficient explorability of groundwater and related resources. *Acta Geophys.* **70**, 1223–1239. https://doi.org/10.1007/s11600-022-00794-8.

George, N. J., Ekanem, A. M., Thomas, J. E., & Harry, T. A. (2022b). Modelling the effect of geo-matrix conduction on the bulk and pore water resistivity in hydrogeological sedimentary beddings. *Modeling Earth Systems and Environment*, 8, 1335–1349. https://doi.org/10.1007/s40808-021-01161-0

George, N. J., Umoh, J. A., Ekanem, A. M., Agbasi, O. E., Jamal, A., & Thomas, J. E. (2022c). Geophysical-laboratory data integration for estimation of groundwater volumetric reserve of a coastal hinterland through optimized interpolation of interconnected geo-pore architecture. *Journal of Coastal Conservation*, 26, 56. https://doi.org/10.1007/s11852-022-00902-2

George, N., Udoinyang, I., Ekanem, A., Udosen, N.& Thomas, J. (2026a). Geoelectrical characterization of aquifer systems for sustainable WASH infrastructure development in coastal Akwa Ibom State, Nigeria. Discover Water. https://doi.org/10.1007/s43832-026-00436-w.

George, N. J., Ekanem, K. R. Ekanem, A. M., Udosen, N. I., Thomas, J. E. (2026b). Geoelectric curve amplitude and percentage thickening for aquifer vulnerability and hydrological connectivity in aquifer-water channel systems: Machine learning performance metrics in Akwa Ibom State. *Geosystems and Geoenvironment*, 5 (4), 100550, https://doi.org/10.1016/j.geogeo.2026.100550

George, N. J., Nathaniel E. U. & Etuk, S. E. (2014). Assessment of Economically Accessible Groundwater Reserve and Its Protective Capacity in Eastern Obolo Local Government Area of Akwa Ibom State, Nigeria, Using Electrical Resistivity Method. *Hindawi*, 2014(3), 1-10

George, N. J., Ibuot, J. C., Ekanem, A. M. & George, A. M. (2018). Estimating the indices of inter-transmissibility magnitude of active surficial hydrogeologic units in Itu, Akwa Ibom State, southern Nigeria. *Arab J Geosci*. 11, 134 (2018). https://doi.org/10.1007/s12517-018-3475-9

George, N. J., Ekanem, A. M., Thomas, J. E. & Ekong, S. A. (2021). Mapping depths of groundwater - level architecture: implications on modest groundwater-level declines and failures of boreholes in sedimentary environs. *Acta Geophys*. 69, 1919–1932. https://doi.org/10.1007/s11600-021-00-663-w

George, N. J., & Thomas, J. E. (2024) Typification of coastal depositional lithofacies with isophysical and isochemical hydro-sand beds via stratigraphic modified Lorenz plots (SMLP): geohydrodynamical implications and valorization of hydrogeological units. *Acta Geophys*. **72**, 1275–1291. https://doi.org/10.1007/s11600-023-011-60-y

George, N. J., & Thomas, J. E. (2023) Groundwater potential and quality assessments of a coastal environment: a case study of the location of Federal University of Technology Ikot Abasi (FUTIA), Akwa Ibom State, Nigeria. *Journal of Coastal Conservation*, 27, 31. https://doi.org/10.1007/s11852-023-009-56-w

Ghazavi, R., & Ebrahimi, Z. (2019). Assessing groundwater vulnerability to contamination using a modified DRASTIC model in an arid climate. *Groundwater for Sustainable Development*, 8, 310 – 319.

Hastie, T., Tibshirani, R., & Friedman, J. (2009). The Elements of Statistical Learning: Data Mining, Inference, and Prediction (2nd ed.). Springer Science and Business Media, New York.

Ikpe, E. O., Ekanem, A. M., George, N. J. Thomas, J. E. & Udosen, N.I. (2025). GOD - and DRASTIC - based valuation of groundwater vulnerability to contamination of hinterland aquifers of northern part of Akwa Ibom State, Nigeria, Results in Earth Sciences 3, 100104, https://doi.org/10.1016/j.rines.2025.100104

Inyang, N. E., Ehibor, I. U., Ekot, A. E., & Udo, I. G. (2024a). An environmental assessment and a priori implications of field investigations of older MSW at Uyo and Younger MSW at Eket, Akwa Ibom State, southern Nigeria. *Researchers Journal of Science and Technology*, 4(1), 45–71. https://doi.org/10.83080/rejost.vol4no1.91

Inyang, N. E., George, N. J., Ehibor, I. U., Ekot, A. E., & Udo, I. G. (2024b). Ingress of municipal solid waste into water resources: an environmental assessment and monitoring tool near dumpsites in Akwa Ibom State, Nigeria. *Water Practice and Technology*, 19(8), 3182–3202.

Isaiah, T., Ekanem, I., & Bello, A. (2021). Delineation of aquifer vulnerability using Dar-Zarrouk parameters in parts of the Anambra Basin, Nigeria. *Journal of African Earth Sciences*, 184, Article 104332.

Jain, A. K. (2010). Data clustering: 50 years beyond K-means. *Pattern Recognition Letters*, 31(8), 651–666.

Kaufman, L., & Rousseeuw, P. J. (1990). Finding Groups in Data: *An Introduction to Cluster Analysis*. John Wiley and Sons, New York.

Kazakis, N., and Voudouris, K. (2017). Groundwater vulnerability and pollution risk assessment of porous aquifers to nitrate contamination using GIS and AHP techniques. *Journal of Hydrology*, 554, 303–318.

Lodwick, W. A., Monson, W., & Svoboda, L. (1990). Attribute error and its propagation in overlay analysis. *International Journal of Geographical Information System*, 4(4), 413–427.

Machiwal, D., Jha, M. K., & Malano, H. M. (2016). Assessment of groundwater vulnerability to pollution using GIS-based modified DRASTIC models in an arid region of India. *Environmental Earth Sciences*, 75, 781. https://doi.org/10.1007-/s12665-016-5590-z

Motlagh, M. B., Nakhaei, M., & Moghaddam, A. A. (2023). Groundwater vulnerability mapping using machine learning models and optimization techniques. *Environmental Science and Pollution Research*, 30(12), 34120–34138.

Napolitano, P., & Fabbri, A. G. (1996). Single-parameter sensitivity analysis for aquifer vulnerability assessment using DRASTIC and GIS. *Application of Geographic Information Systems in Hydrology and Water Resources Management*, IAHS Publication No. 235, 559–566.

Obianwu, V., George, N. & Udofia, K. (2011). Estimation of aquifer hydraulic conductivity and effective porosity distributions using laboratory measurements on core samples in the Niger Delta, Southern Nigeria, International Review of Physics, 5(1), 19-24.

Oki, O. A., & Akamigbo, F. O. R. (2020). Lithostratigraphy and hydrogeological characterization of the Ameki Formation, Southeastern Nigeria. *African Journal of Geosciences*, 15(2), 112–125.

Piscopo, G. (2001). Groundwater vulnerability map explanatory notes, Castlereagh catchment. Department of Land and Water Conservation, Australia.

Rousseeuw, P. J. (1987). Silhouettes: A graphical aid to the interpretation and validation of cluster analysis. *Journal of Computational and Applied Mathematics*, 20, 53–65.

Saaty, T. L. (1980). The analytic hierarchy process: Planning, priority setting, resource allocation. McGraw-Hill.

Shannon, C. E. (1948). A mathematical theory of communication. *The Bell System Technical Journal*, 27(3), 379–423.

Thomas, J. E., Udosen, N. I., Ekanem, A. M. & George, N. J. (2025). Hydrogeological and electrostratigraphic modeling of coastal aquifers: Investigating systemic vulnerability, hydraulic yield potential, and corrosivity pathways. *Solid Earth Sciences*, 10(2), 100243

Thorndike, R. L. (1953). Who belongs in the family? *Psychometrika*, 18(4), 267–276.

Udo, I. G., & Mode, A. W. (2013). Use of statistical parameters in the sedimentological study of conglomerate deposits in northeastern part of Akwa Ibom State, Niger Delta Basin, Nigeria. *IOSR Journal of Applied Geology and Geophysics*, 1(5), 21–27.

Udo, I. G., Udofia, P. A., Etukudo, N. J., and Adesina, D. A. (2023). Paleo-environmental interpretation of the exposed section of the Benin Formation in southeastern part of the Niger Delta Basin, Nigeria: A pebble morphometric approach. *IOSR Journal of Applied Geology and Geophysics*, 11(3 Ser. III), 12–19.

Udosen, N. I., Ekanem, A. M., & George, N. J. (2024a). Appraisal of flood-prone litho-stratigraphic units via geo electrical technology. *Malaysian Journal of Geosciences*, 8(1), 26–37.

Udosen, N. I., Ekanem, A. M., & Thomas, J. E. (2023). Evaluation and modeling of a major coastal aquifer's vulnerability to contamination with the use of GOD and AVI models as indicators in South-eastern Nigeria. *Researchers Journal of Science and Technology*, 3(4), 61–78. https://-doi.org/10.83080/rejost.vol3no4.80

Udosen, N. I., Ekanem, A. M., and Thomas, J. E. (2024b). Geo-electrostratigraphic assessment of aquifer potential, protectivity, and pliable level of vulnerability within a coastal milieu. *Water Practice and Technology*, 19(5), 2010–2031. https://doi.org/10.2166/wpt.-2024.125

Udosen, N. I., Ekanem, A. M., & Thomas, J. E. (2024c). Geo-hydraulic characterization of a coastal aquifer system in South-eastern Nigeria with the inverse slope method. *Researchers Journal of Science and Technology*, 4(1), 1 – 20. https:-//doi.org/10.83080/rejost.vol4no1.82

Udosen, N. I. & George, N. J. (2018) Characterization of electrical anisotropy in North Yorkshire, England using square arrays and electrical resistivity tomography. *Geomech. Geophys. Geo-energ. Geo-resour.* 4, 215–233. https:-//doi.org/10.1007/s40948-018-0087-5.

Udosen, N. I., Ekanem, A. M., & George, N. J., (2024d). Modeling of aquifer geo-hydraulic characteristics with geo-electrical methods at a major coastal aquifer system in Uyo, southern Nigeria. *Water Practice and Technology* (2024) 19 (2): 611 – 628. https://doi.org/10.2166-/wpt.2024.018

Udosen, N. I., Ekanem, A. M., & George N. J. (2024e). Geophysical exploration to assess leachate percolation and aquifer protectivity within hydrogeological units at a major open dump in Eket, Nigeria. *Results in Earth Sciences*, 2, 100022, ISSN 2211-7148, https://doi.org/10.1016-/j.rines.2024.100022.

Umoh, J. A., George, N. J., Ekanem, A.M. & Emah J. B. (2025). Characterization of hydro-sand beds and their hydraulic flow units by integrating surface measurements and ground truth data in parts of the shorefront of Akwa Ibom State, Southern Nigeria. *Int J Energ Water Res* 9, 13–290. https://doi.org/10.1007/s42108-022-002-15-y

Umoh, J. A., George, N. J., Ekanem, A. M., Thomas, J. E., & Emah, J. B. (2022). Approximate delineation of groundwater yield capacity and vulnerability via secondary geo-electric indices and rock-water interaction hydrodynamic coefficients in a coastal environment. *Researchers Journal of Science and Technology*, *2*(3), 28–54. https://doi.org/10.83080/rejost.vol2no3.40

Uwa, U.E., Akpabio, G.T. & George, N.J. (2019) Geohydrodynamic Parameters and their Implications on the Coastal Conservation:

A Case Study of Abak Local Government Area (LGA), Akwa Ibom State, Southern Nigeria. *Nat Resour Res* **28**, 349–367 (2019). https://doi.org/10.1007/s11053-018-9391-6

Uzcategui-Salazar, M., & Lillo, M. (2025). Application of unsupervised machine learning algorithms for automated hydrogeological risk zonation. *Journal of Environmental Management*, 351, 119820.